

ABSTRACT

Title of Document: PARAMETRIC STUDY OF SYNTHETIC JET
ACTUATORS ON A BACKWARD FACING
STEP

Aaron M. Sassoon, Master of Science , 2013

Directed By: Langley Distinguished Professor,
Dr. James E. Hubbard, Jr.,
Department of Aerospace Engineering

Associate Dean of Research and Professor,
Dr. Alison Flatau,
Department of Aerospace Engineering

The ability of synthetic jet actuators to leverage natural instabilities in the flow field due to separation is reviewed for applications towards virtual shape change. The separating flow over a backward facing step of height h is studied under the influence of an actuator upstream and downstream of separation. Experimental tests were conducted in a wind tunnel using particle imaging velocimetry and time-averaged static pressure data to measure and analyze the affected flow fields and pressure distribution. By placing a second actuator downstream of separation, the ability to influence the pressure distribution has been shown. The two actuators demonstrated the ability to affect C_p and $\frac{\partial C_p}{\partial x}$ in the region from $0 - 6h$ after the step.

PARAMETRIC STUDY OF SYNTHETIC JET ACTUATORS ON A BACKWARD
FACING STEP

By

Aaron M. Sassoon

Thesis submitted to the Faculty of the Graduate School of the
University of Maryland, College Park, in partial fulfillment
of the requirements for the degree of
Master of Science
2013

Advisory Committee:
Professor James E. Hubbard, Chair/Advisor
Professor Alison Flatau, Chair/Advisor
Professor Allen E. Winkelmann

© Copyright by
Aaron M. Sassoon
2013

Dedication

To both of my parents, grandparents, and nana for all of their full love and support throughout this entire process.

Acknowledgements

I would like to thank a few people and organizations that have helped me along the way and helped make this work possible. My colleague Zohaib Hasnain who throughout the entire process has been instrumental in helping me out and providing assistance. I owe the utmost gratitude to Dr. Alison Flatau and Dr. James E. Hubbard for their guidance and support throughout my graduate years. I hope to continue correspondence with both of them and look forward to future collaborations. Andrew Lind for his advice and the Anya Jone's Lab for lending out the PIV system. Jose Mondragon, Brian Pinto, Lauren Trollinger, Samanth Walters, and Rosie Weinstein for their cooperation and help with various testing. The contributions of Alexander Brown who laid the foundations of this project by authoring the NSF proposal that is funding this work. The aid and advice of Dr. Alan E. Winkelmann and Dan J. Clingman of the Boeing Corporation. Lastly, the National Science Foundation which provided the funding, under NSF Award # 1031077 Dynamical Systems, GOALI, Fluid Dynamics.

Table of Contents

Dedication	ii
Acknowledgements.....	iii
Table of Contents	iv
List of Tables	vi
List of Figures	vii
Chapter 1: Introduction - Overview	1
Section 1.1 Active vs. Passive Flow Control.....	1
Section 1.2 Synthetic Jet actuators - Function/applications.....	2
Section 1.3 Virtual Aeroshaping.....	3
1.4 Flow Over Backward Facing Step	5
1.5 Flow Control Over Backward Facing Step.....	7
1.6 Overview and Objective of this Research.....	8
Chapter 2: Experimental Methodologies	11
2.1 Synthetic Jet Actuator	11
2.2 Closely Spaced Synthetic Jet Actuator Array.....	14
2.3 Wind Tunnel Experimental Setup.....	16
2.4 Overview of Experimental Test 1: Single Actuator Upstream	19
2.5 Overview of Experimental Test 2: Actuator Upstream and Downstream of Backward Facing Step	22
2.6 Computational Study of Flow Over Backward Facing Step.....	24
Chapter 3: Results of Experimental Test 1: Single Actuator Upstream	26
3.1 Backward Facing Step with Single Actuator Upstream	26
3.2 Actuator Location	27
3.3 Boundary Layer State Before Separation	28
3.4 Assessing Reattachment: Forward Flow Probability	30
3.5 Length of Separated Flow Over Backward Facing Step.....	31
3.6 Strouhal Number of Flow Over a Backward Facing Step	32
3.7 Time-Averaged PIV Results	33
Chapter 4: Results of Experimental Test 2: Actuator upstream and downstream	37

4.1	Scaling of $F +$	37
4.2	Location of SJA2	38
4.3	Momentum Coefficient $C_{\mu 1}$ & $C_{\mu 2}$	39
4.4	Computational Results of Flow Over a Backward Facing Step	40
4.6	Experimental Test 2 Results: Pressure Coefficient.....	42
4.7	Pressure Coefficient Results in Region III.....	45
4.8	Pressure Coefficient Results in Region I	50
4.9	Pressure Coefficient Results in Region II.....	59
	Chapter 5: Conclusion and Summary	69
	Appendices.....	71

List of Tables

Table 1: Reduction in Separation Length for Different Values of SJA1 location, \mathbf{XR}	35
Table 2: Standard Deviation in 1 st order Approximation of $\partial \mathbf{Cp} \partial \mathbf{x}$ for Region III..	48
Table 3: Standard Deviation in 1 st order Approximation of $\partial \mathbf{Cp} \partial \mathbf{x}$ for Region I	57
Table 4: Standard Deviation in 1 st order Approximation of $\partial \mathbf{Cp} \partial \mathbf{x}$ for Region II – Section 1.....	65
Table 5: Standard Deviation in 1 st order Approximation of $\partial \mathbf{Cp} \partial \mathbf{x}$ for Region II – Section 2.....	67

List of Figures

Figure 1 (Left) SJA during outflow (Right) SJA during inflow	2
Figure 2 Airfoil model showing an inset with the interaction domain between the jet and the cross flow (Chatlynne et al.)	4
Figure 3 Flow over a backward facing step illustrating parameters associated with periodicity of shed vortices and flow instabilities	7
Figure 4 Illustration of experimental test parameters for study of upstream actuator position on influencing the separation length XR	9
Figure 5 Illustration of experimental test parameters for study of influence of downstream actuator position on region of separated flow	10
Figure 6 Exploded view of synthetic jet actuator	11
Figure 7 Dimensions of Synthetic Jet Actuator	12
Figure 8 Frequency response of synthetic jet actuator.....	14
Figure 9 3-D model of closely spaced synthetic jet actuator array.....	15
Figure 10 Average magnitude of velocity profile of synthetic jet actuator array configuration shown in Figure 9.....	15
Figure 11 3D CAD model of step with dimensions.....	17
Figure 12 Close up of 3D CAD model center cut out with dimensions	17
Figure 13 Photograph of experimental setup installed inside the test section of the wind tunnel. High speed camera location and actuator locations are denoted in the above figure	18
Figure 14 Experimental setup inside of the wind tunnel with laser sheet. (b) Enlarged view of actuator location before and after step.....	20
Figure 15 Photograph of experimental laser test setup.....	21
Figure 16 Step model with layout of static pressure ports along bottom wall.....	22
Figure 17 3-D CAD model of plastic pressure port plates illustrated with synthetic jet actuator.....	23
Figure 18 Illustration of computational model with boundary conditions	25
Figure 19 Average magnitude of velocity profile of synthetic jet actuators.....	26
Figure 20 Illustration of experimental test parameters for experimental test 1 with specified dimensions.....	28
Figure 21 Time averaged experimental PIV results for flow over backward facing step without synthetic jet actuation. Red box indicates region used to assess the boundary layer height	30

Figure 22 Computational results for flow over a backward facing step illustrating length of separation bubble.....	32
Figure 23 a-e. Average PIV velocity magnitude plots $Reh \approx 7800$ (a) Baseline case without actuation (b) actuator distance $Xs = 1.07h$ (denoted by white arrow). (b) actuator distance $Xs = 2.14h$ (denoted by white arrow). (c) actuator distance $Xs = 4.28h$. (d) actuator distance $Xs = 7.14h$	36
Figure 24 Illustration of experimental test parameters for second study with dimensioned actuator locations.....	39
Figure 25 Pressure coefficient downstream of backward facing step from numerical results (dashed line) and experimental results (solid line).....	41
Figure 26 Illustration of the three different regions shown in the results of the pressure coefficient downstream of the step.....	42
Figure 27 Format of results that will be presented (a) $C\mu_2 = .02$ (b) $C\mu_2 = .094$. for all three regions. (Only Region II shown above for illustration purposes).....	44
Figure 28 Region III $XSD = .75h$ – Pressure coefficient downstream of step with varying momentum coefficient for SJA2, $C\mu_2$. (a) Constant momentum coefficient for SJA1, $C\mu_2 = .02$ (b) Constant momentum coefficient for SJA1, $C\mu_2 = .094$	45
Figure 29: Region III $XSD = 2.68h$ – Pressure coefficient downstream of step with varying momentum coefficient for SJA2, $C\mu_2$. (a) Constant momentum coefficient for SJA1, $C\mu_2 = .02$ (b) Constant momentum coefficient for SJA1, $C\mu_2 = .094$	46
Figure 30: Region III $XSD = 4.63h$ – Pressure coefficient downstream of step with varying momentum coefficient for SJA2, $C\mu_2$. (a) Constant momentum coefficient for SJA1, $C\mu_2 = .02$ (b) Constant momentum coefficient for SJA1, $C\mu_2 = .094$	47
Figure 31: $XSD = .75h$ – First order approximation of $\partial Cp/\partial x$ versus $C\mu_1$ for different values of $C\mu_2$ in Region III.....	48
Figure 32: $XSD = 2.68h$ – First order approximation of $\partial Cp/\partial x$ versus $C\mu_1$ for different values of $C\mu_2$ in Region III.....	49
Figure 33 Region I $XSD = .75h$ – Pressure coefficient downstream of step with varying momentum coefficient for SJA2, $C\mu_2$. (a) Constant momentum coefficient for SJA1, $C\mu_2 = .02$ (b) Constant momentum coefficient for SJA1, $C\mu_2 = .094$	53
Figure 34 Region I $XSD = 2.68h$ – Pressure coefficient downstream of step with varying momentum coefficient for SJA2, $C\mu_2$. (a) Constant momentum coefficient for SJA1, $C\mu_2 = .02$ (b) Constant momentum coefficient for SJA1, $C\mu_2 = .094$	54
Figure 35 Region I $XSD = 4.63h$ – Pressure coefficient downstream of step with varying momentum coefficient for SJA2, $C\mu_2$. (a) Constant momentum coefficient for SJA1, $C\mu_2 = .02$ (b) Constant momentum coefficient for SJA1, $C\mu_2 = .094$	55
Figure 36 $XSD = .75h$ – First order approximation of $\partial Cp/\partial x$ versus $C\mu_1$ for different values of $C\mu_2$ in Region I.....	58

Figure 37 $XSD = 2.68h$ – First order approximation of $\partial C_p \partial x$ versus $C_{\mu 1}$ for different values of $C_{\mu 2}$ in Region I..... 58

Figure 38 $XSD = 4.63h$ – First order approximation of $\partial C_p \partial x$ versus $C_{\mu 1}$ for different values of $C_{\mu 2}$ in Region I..... 59

Figure 39 Region II $XSD = .75h$ – Pressure coefficient downstream of step with varying momentum coefficient for SJA2, $C_{\mu 2}$. (a) Constant momentum coefficient for SJA1, $C_{\mu 2}=.02$ (b) Constant momentum coefficient for SJA1, $C_{\mu 2}=.094$ 61

Figure 40 Region II $XSD = 2.68h$ – Pressure coefficient downstream of step with varying momentum coefficient for SJA2, $C_{\mu 2}$. (a) Constant momentum coefficient for SJA1, $C_{\mu 2}=.02$ (b) Constant momentum coefficient for SJA1, $C_{\mu 2}=.094$ 62

Figure 41 Region II $XSD = 4.63h$ – Pressure coefficient downstream of step with varying momentum coefficient for SJA2, $C_{\mu 2}$. (a) Constant momentum coefficient for SJA1, $C_{\mu 2}=.02$ (b) Constant momentum coefficient for SJA1, $C_{\mu 2}=.094$ 63

Figure 42 $XSD = .75h$ – First order approximation of $\partial C_p \partial x$ versus $C_{\mu 1}$ for different values of $C_{\mu 2}$ in Region II – Section 1 (2.5h-4h) 66

Figure 43 $XSD = 4.63h$ – First order approximation of $\partial C_p \partial x$ versus $C_{\mu 1}$ for different values of $C_{\mu 2}$ in Region II – Section 1 (2.5h-4h) 66

Figure 44 $XSD = .75h$ – First order approximation of $\partial C_p \partial x$ versus $C_{\mu 1}$ for different values of $C_{\mu 2}$ in Region II – Section 2 (3.5h-5h) 68

Figure 45 $XSD = 2.68h$ – First order approximation of $\partial C_p \partial x$ versus $C_{\mu 1}$ for different values of $C_{\mu 2}$ in Region II – Section 2 (3.5h-5h) 68

Figure 46 $XSD = 1.63h$ – Pressure distribution downstream of step with varying momentum coefficient for SJA2, $C_{\mu 2}$. (a) Constant momentum coefficient for SJA1, $C_{\mu 2}=.02$ (b) Constant momentum coefficient for SJA1, $C_{\mu 2}=.094$ 71

Figure 47 $XSD = 3.63h$ – Pressure distribution downstream of step with varying momentum coefficient for SJA2, $C_{\mu 2}$. (a) Constant momentum coefficient for SJA1, $C_{\mu 2}=.02$ (b) Constant momentum coefficient for SJA1, $C_{\mu 2}=.094$ 72

Chapter 1: Introduction - Overview

Section 1.1 Active vs. Passive Flow Control

In the aerospace industry there is always an effort to find new ways to fly faster, farther and more efficiently. Active flow control offers the ability to revolutionize aircraft design, improving performance capability by simplifying complex control surfaces, and reducing weight. The study of flow control involves manipulating flow fields in order to modify their aerodynamic characteristics and satisfy a selected performance metric. Over the past few decades, research and technology advancements have paved the way for the use of an active flow control device called a Synthetic Jet Actuator (SJA) (Glezer 2011). SJAs or zero net mass-flux devices are small lightweight devices that can be described in the simplest terms, as a sealed cavity with an oscillating diaphragm and a small opening on one side of the cavity. As the diaphragm moves up and down, the change in cavity volume induces an expulsion and ingestion of air through the orifice. A simplified illustration of a synthetic jet actuator is shown in Figure 1. With careful design of the orifice for operational parameters (e.g. frequency, displacement) a vortex pulse train through the orifice is created that coalesces into a jet of air.

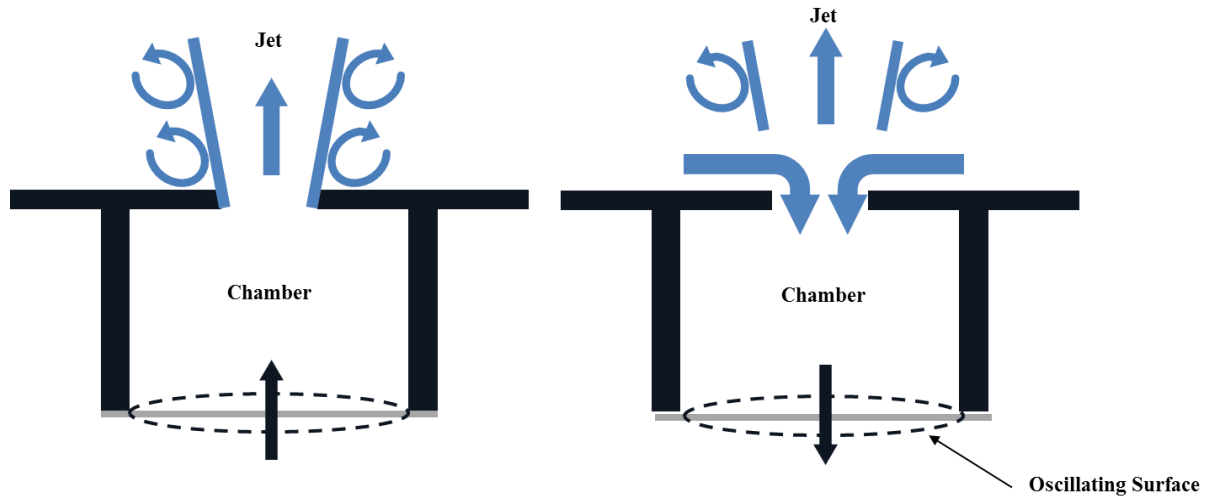


Figure 1 (Left) SJA during outflow (Right) SJA during inflow

Section 1.2 Synthetic Jet actuators - Function/applications

During the late 90's and on through to the early 2000's there have been numerous review articles regarding the function and application of SJAs (Greenblatt and Wygnanski 2000, Glezer and Amitay 2002, Glezer 2011). Synthetic jet actuators have been used for flow control applications such as boundary layer separation control and virtual aerodynamic shaping. Boundary layer separation control through periodic excitation has been an interest of many researchers since the 1980's. Experiments have shown that acoustic excitation of the separating shear layer at a forcing frequency that is close to the natural shedding frequency, $St_{act} \sim O(St_s)$, will delay the onset of separation and stall at high angles of attack (Greenblatt & Wygnanski 2000). Subsequently, Glezer and Amitay proposed excitation at a frequency that is at least an order of magnitude higher than the natural shedding frequency of the flow, $St_{act} \sim O(10St_s)$. They noted that forcing close to the natural shedding frequency of the shear layer can cause instabilities in the flow field resulting

in unsteady aerodynamic forces (Glezer & Amitay 2002). By forcing at a frequency $St_{act} \sim O(10St_s)$ or higher, the forcing frequency no longer remains coupled to any resonant frequency in the flow, avoiding any instability that may arise as a result. This also eliminates the limited bandwidth associated with forcing near the characteristic frequency of the flow. When at $\sim 10St_s$ or higher, an interaction domain develops between the jet and the cross flow which results in a closed form recirculation region upstream of separation. This recirculation region alters the streamwise pressure gradient to delay or suppress any flow detachment that would have otherwise occurred (Honohan 2000 & Glezer et al 2003). The closed form recirculation that develops becomes a virtual shape, displacing the local streamlines.

Section 1.3 Virtual Aeroshaping

The virtual shaping of airfoils has been an interest of researchers for many years. Synthetic jet actuators can also be used to virtually shape the airfoil thus increasing performance metrics and extending the aerodynamic profile with minimal added structural weight. Chatlynne et al. demonstrated the use of synthetic jet actuators for fluidic shape modification on a Clark-Y airfoil at low angles of attack, yielding a small reduction in pressure drag. Placing a synthetic jet actuator directly downstream of a passive obstruction creates a recirculation region next to the surface of the airfoil as shown in Figure 2. A synthetic jet actuator with a miniature obstruction was located on the suction side of a Clark-Y airfoil. Similarly a study by Chen and Beeler showed that a reduction in lift occurs on the airfoil as compared to

the baseline case for a NACA 0015 using only a synthetic jet actuator and no obstruction. Desalvo and Glezer were able to demonstrate an increase in lift and a reduction in pressure drag with a wedge-like obstruction in combination with a synthetic jet. By placing one of these ‘hybrid’ actuators near the leading edge and another one by the trailing edge on the pressure side of the airfoil, they were able to trap vortex concentrations close to the surface, which was then used to alter the Kutta condition of the airfoil. They were also able to show increases in L/D_p using this method. Shea et al. produced similar results using a synthetic jet actuator behind a gurney flap in order to modify the wake of a gurney flap and consequently alter the Kutta condition.

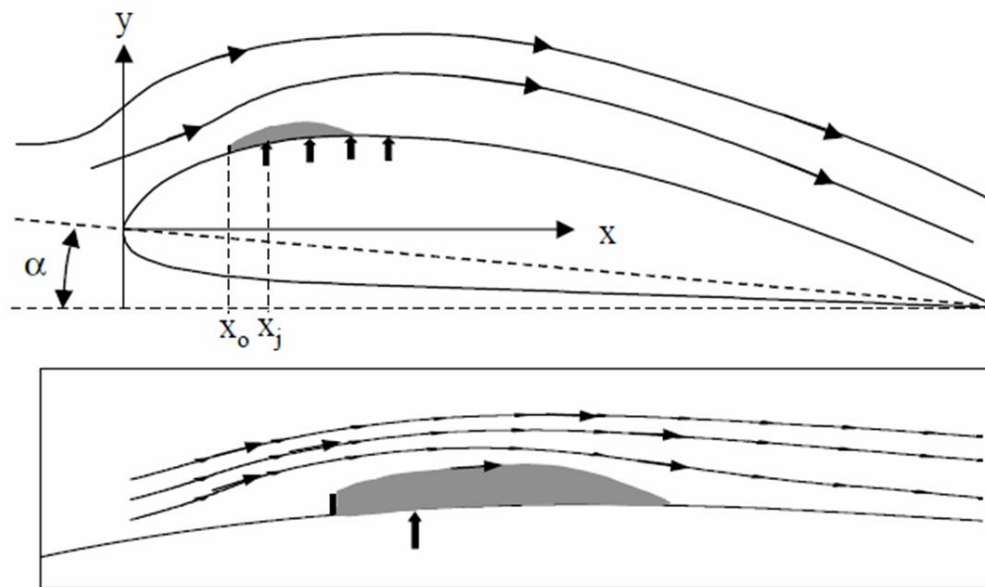


Figure 2 Airfoil model showing an inset with the interaction domain between the jet and the cross flow (Chatlynne et al.)

The works cited above on virtual shaping have all focused on altering the shape of current airfoil designs; however, none have explored the notion that with

virtual shaping, airfoil design can transition away from being a compromise and move towards a fundamentally novel kind of airfoil. Looking forward, aircraft designers can eliminate such compromises by employing an active flow control device to change the airfoil shape on demand. In order to do so, there needs to be a more comprehensive understanding of virtual shaping using synthetic jet actuators.

Given the brief literature review presented above, it is evident that some mechanism, either fluidic or geometric, is necessary to displace the local streamlines and cause separation. Consequently, this resulting region of recirculation can be manipulated by placing a synthetic jet actuator directly in the wake of the region of separated flow.

1.4 Flow Over Backward Facing Step

A simple and commonly encountered geometry for separated flow is shown in the flow over a Backward Facing Step (BFS). From automobiles to aircraft, to buildings, all have in some shape or form a backward facing step. Separated flows are an important flow phenomenon to study because they cause drag and unsteady aerodynamic forcing which can lead to fatigue. In the field of aerodynamics, the flow over a backward facing step has been studied for over 60 years. It represents a building block for all other separated flows. The BFS is widely used to study separated flows because the flow will always separate at the step and reattach some distance downstream (Spazzini 2001).

The separated flow can be divided into three primary regions as shown in Figure 3. These are shown as the separated shear layer, the recirculation, and the reattachment zone. The separated shear layer begins to form at the edge of the step between the high moving cross flow and the low velocity flow adjacent to the downstream edge of the step. This is similar to a free shear layer. The separated shear layer differs in behavior from the free shear layer due to the highly turbulent flow on the low speed side of the shear layer. An integral part of the separated shear layer is the roll up of the flow field and the shedding of vortices. There is large body of literature regarding the process and flow physics governing the vortex pairing and shedding (Spazzini, Heenan and Morrison 1996, Driver et al. 1987). The non-dimensional frequency or Strouhal number used to describe oscillating flows associated with vortex shedding for the separated flow over a backward facing step is near 1. The Strouhal number can be defined as:

$$St = \frac{fL}{U_\infty}$$

where f is the frequency associated with the vortex shedding, L is a characteristic reference length, and U_∞ is the cross flow velocity. For the backward facing step, L is taken to be X_R which is the length of mean reattachment region. Some authors have instead used h as a reference length, the height of the step instead of X_R and the Strouhal number associated with it is approximately $St \approx 0.185$ (Hasan). The recirculation region is located below the separated shear layer and is often referred to as the separation bubble. The recirculation region is broken up into the primary

recirculation at the center of this region and secondary recirculation located adjacent to the step as shown in Figure 3.

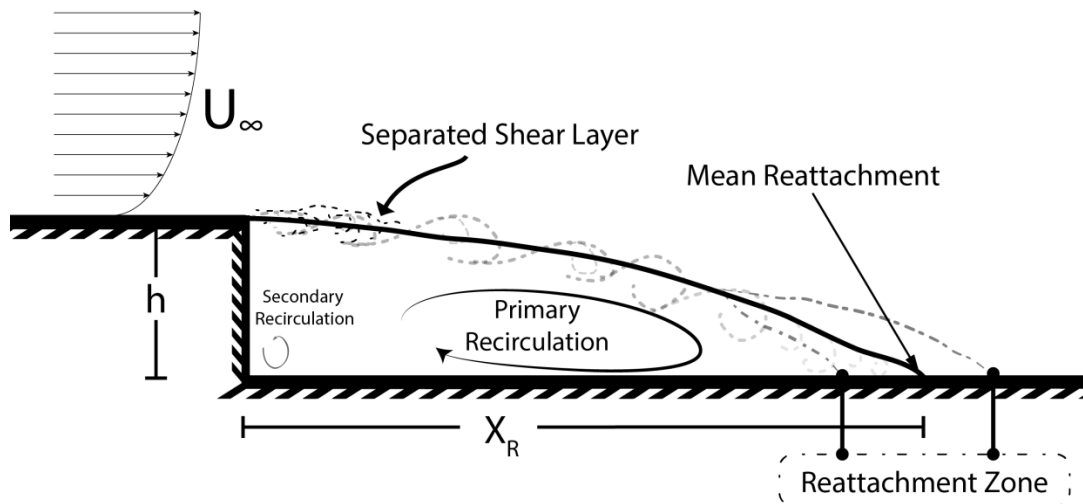


Figure 3 Flow over a backward facing step illustrating parameters associated with periodicity of shed vortices and flow instabilities

1.5 Flow Control Over Backward Facing Step

Flow over a backward facing step will always separate at the step and reattach some distance downstream (Spazzini 2001). The main focus of active flow control on a backward facing step is to influence the length of the reattachment region. Studies of the 1950's, have researched the prospects of introducing local forcing to reduce the size of the separated region (Greenblatt & Wygnanski 2000). Yoshioka et al. employed the use of periodic perturbations introduced at the edge of the step to reduce the separation length by promoting mixing and greater momentum transfer in the shear layer. They found that an optimum frequency corresponding to $St=1.9$ reduced the separation length by 30%. The optimum perturbation frequency was approximately twice that of the dominant frequency in the flow, i.e. the shedding

frequency. Yamada et al. demonstrated the use of synthetic jet actuators for periodic perturbation directly upstream of the step in order to control the location of reattachment region. More recently, Yasuhiro et al. explored the influence of phase differences of a synthetic jet actuator array on altering the reattachment process. Two synthetic jet actuators were located at a distance of $11.25h$ upstream from the step and spaced $7.5h$ apart in the spanwise direction. The perturbation frequency was chosen to coincide with the dominant frequency associated with the shedding shear layer. All of the above work focused on a forcing frequency that was close to the natural frequency of the shedding shear layer $St_{act} \sim O(St_s)$, Vukasinovic et al. investigated the effect of higher frequency forcing $St_{act} \sim O(10St_s)$. As discussed earlier, forcing close to the dominant frequency in the flow can lead to instabilities in the flow field resulting in unsteady aerodynamic forces. Vukasinovic et al. showed high frequency actuation leads to enhanced turbulent kinetic energy and the transfer of turbulent kinetic energy from large scales to small scales. As opposed to direct forcing of the shear layer, an interaction domain upstream of separation is formed that induces this increase in mixing.

1.6 Overview and Objective of this Research

Recent work by Desalvo et al. (2011) showed a positive influence of multiple actuators, placed adjacent to each other in affecting flow reattachment over a drooped flap. Building upon this notion, the main objective of this research is to conduct a parametric study of the influence of synthetic jet actuators on flow over a backward facing step.

The work presented herein studies the effect of synthetic jet actuators on the flow over a backward facing step at forcing frequencies which are at least an order of magnitude higher than the natural frequency of the shedding shear layer, $St_{act} \sim O(10St_s)$, investigating the interacting flow domain between two synthetic jet actuators and a backward facing step. A single actuator placed upstream of separation has been shown to alter the streamwise pressure gradient in a manner to delay separation (Glezer et al 2003). One objective of this work is to investigate the influence of a second actuator placed downstream of the step on the region of separated flow.

1.6.1 Experimental Overviews

Two separate sets of experiments were conducted. The first set studied the effect of actuator placement upstream of the step on the flow reattachment length as shown in Figure 4. Four discrete locations upstream from the step were tested denoted as in Figure 4 as X1-X4.

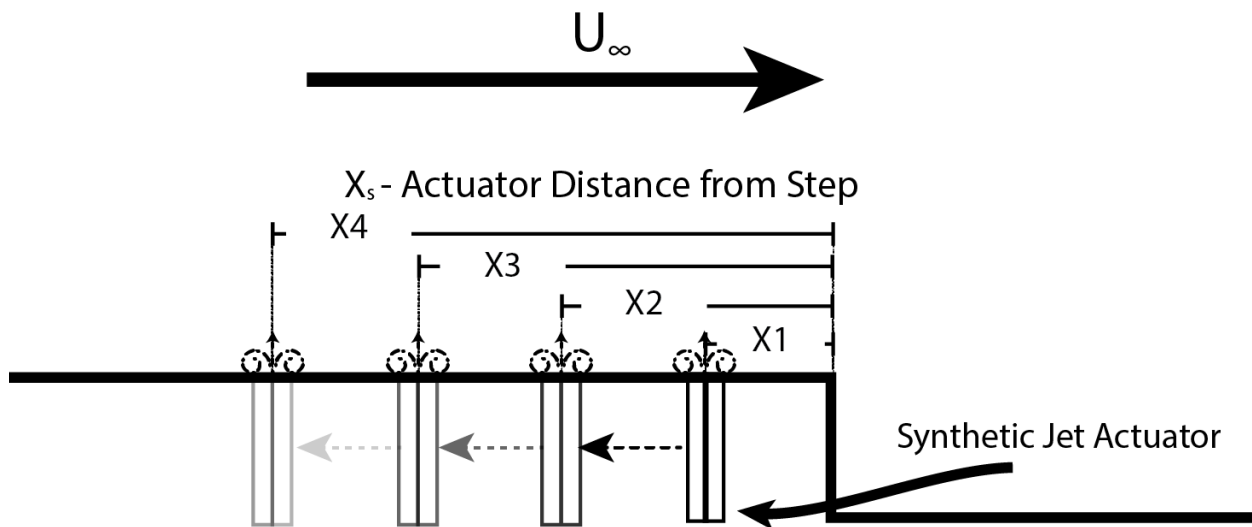


Figure 4 Illustration of experimental test parameters for study of upstream actuator position on influencing the separation length X_R

The objective here was to establish a baseline flow in which a second actuator placed downstream of the step could influence the region of recirculating flow and thus create an interaction domain. The second study was initiated to observe the combined influence of two actuators on the flow. The location of the actuator placed upstream of the step was kept constant and the location of the downstream actuator was placed at 5 different locations downstream from the step shown in Figure 5 as X1-X5. The first actuator, placed upstream of the step is referred to as SJA1; the second actuator, placed downstream of the step is referred to as SJA2 as shown in Figure 5.

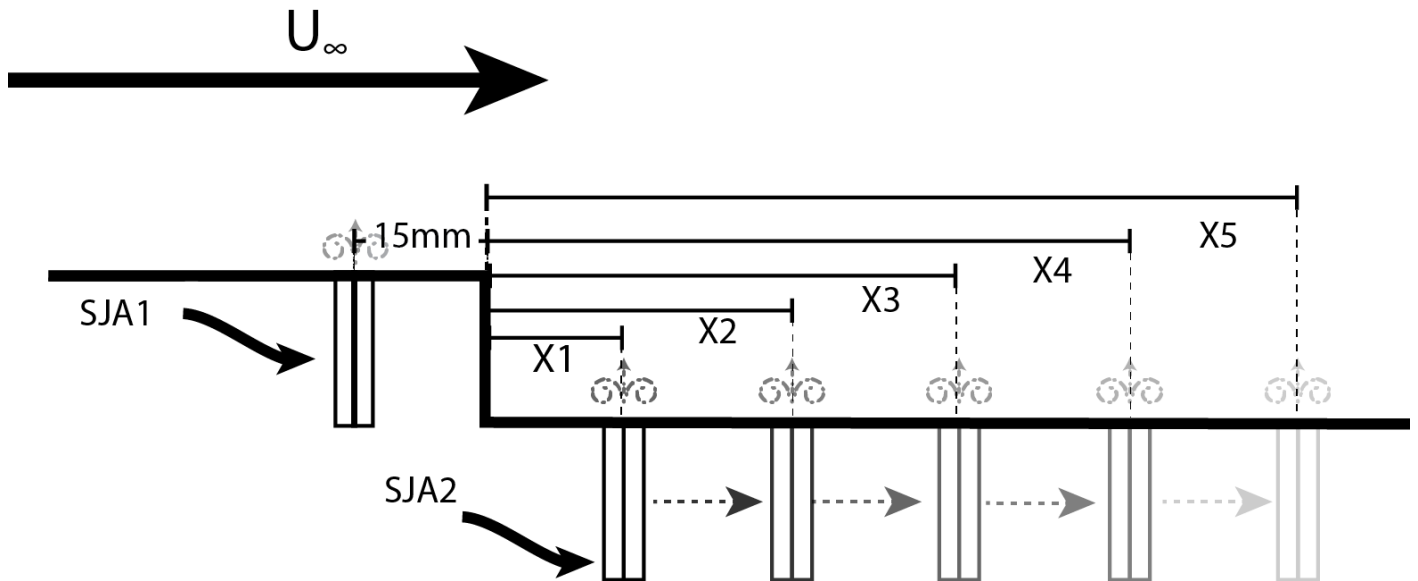


Figure 5 Illustration of experimental test parameters for study of influence of downstream actuator position on region of separated flow

Chapter 2: Experimental Methodologies

2.1 Synthetic Jet Actuator

2.1.1 Design CAD Layout – Overview – Construction

The synthetic jet actuators used in the experiments presented here were based on a NASA design (Rumsey 2004). An exploded view of the actuator is shown in Figure 6. The housings and clamps for the actuators were machined out of aluminum at the University of Maryland Aerospace machine shop. The actuators were clamped between two O-rings to approximate a pinned boundary condition and the cavity of the housing was sealed with a back plate as noted in Figure 6. High vacuum silicon grease was applied to both O-rings and the lip the actuator sits on in order to provide a strong seal and prevent any leaks which would have a detrimental effect on the actuator performance. The actuators were torqued to 0.5Nm to ensure consistent boundary conditions.

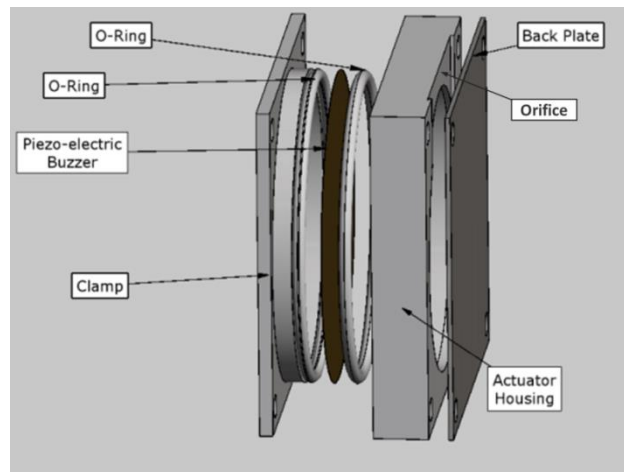


Figure 6 Exploded view of synthetic jet actuator

The actuator housing and clamp dimensions are shown in Figure 7. The actuator housing, clamp, and backplate were 44.4mm x 44.4mm \pm 0.05mm. The width of the clamp was 1.8mm \pm 0.05mm (without the lip section which sits inside the actuator housing when it was assembled). The width of the actuator housing was 7.4mm \pm 0.05mm and the width of the backplate was 0.6mm \pm 0.05mm. The actuator orifice measured 0.5mm x 28mm \pm 0.05mm which yields an aspect ratio of 56. The piezoelectric disk measured 41mm in diameter. The width of the entire assembled actuator was approximately 9.5mm \pm 0.5mm.

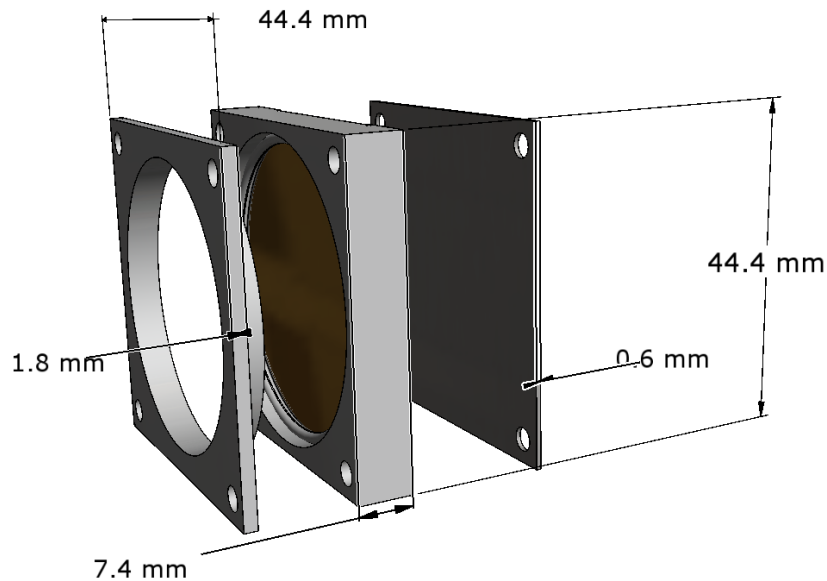


Figure 7 Dimensions of Synthetic Jet Actuator

2.1.2 Synthetic Jet Actuator Characterization

The actuators were characterized using bench top hotwire tests in quiescent conditions to determine their frequency responses. The hotwire tests were conducted using a TSI double channel IFA 300 Constant Temperature Anemometer (CTA) with

a TSI single channel hot film probe, model #1210-20. For the tests, the probe was positioned at the center of the orifice in the spanwise direction and located at a height of $5\text{mm} \pm 0.5\text{mm}$ above the orifice. A function generator was used to supply a sinusoidal drive signal as input to the amplifier. A frequency sweep of the drive signal was conducted from $800\text{Hz} - 2200\text{Hz}$. The data was acquired at a sampling rate of $20,000\text{Hz}$ and a mean value was calculated over 16,000 samples. For each discrete frequency, three mean values were recorded and averaged to acquire the final mean velocity. The standard deviation of the recorded mean was $\pm 0.1\text{ m/s}$.

The actuators were found to have two resonant peaks, as shown in Figure 8. The dominant resonant peak occurred between $1700\text{-}1800\text{Hz}$ and the secondary peak occurred between $1100\text{Hz} - 1200\text{Hz}$. These two peaks are associated with the Helmholtz resonant frequency of the cavity and the structural resonant frequency of the piezoelectric disk. The manufacturer of the piezoelectric disks state that the resonant frequency of the piezoelectric disks was approximately $2200\text{Hz} \pm 0.3\text{kHz}$.

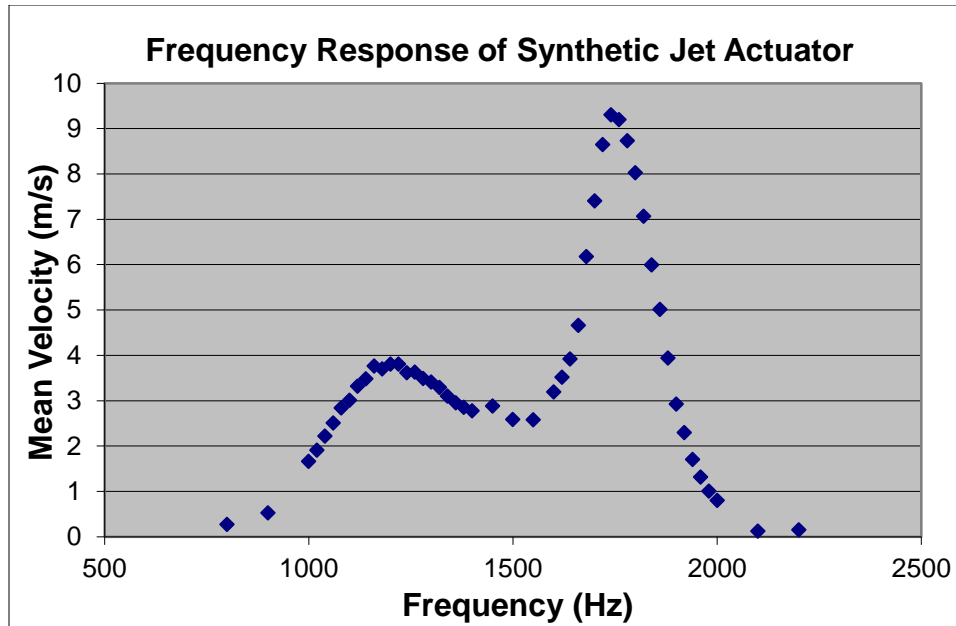


Figure 8 Frequency response of synthetic jet actuator

2.2 Closely Spaced Synthetic Jet Actuator Array

Two individual actuators were paired together, spaced $1.3\text{mm} \pm 0.05\text{mm}$ apart or 2.5 times the orifice width and considered as one single synthetic jet actuator as shown in Figure 9. Hasnain et al. (2012) and Smith and Glezer (2005) showed that the jet profiles of two closely spaced actuators, operated in phase and with matched velocities, will merge to form a single jet.

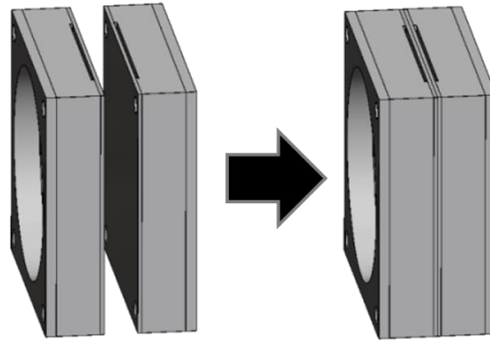


Figure 9 3-D model of closely spaced synthetic jet actuator array

For all the experimental tests, the phase of the actuators was kept constant. Particle Image Velocimetry (PIV) measurements taken under quiescent flow conditions were used to characterize the velocity profile of each jet, and to match the velocities for the pairs of closely spaced actuators. These results are shown in Figure 10.

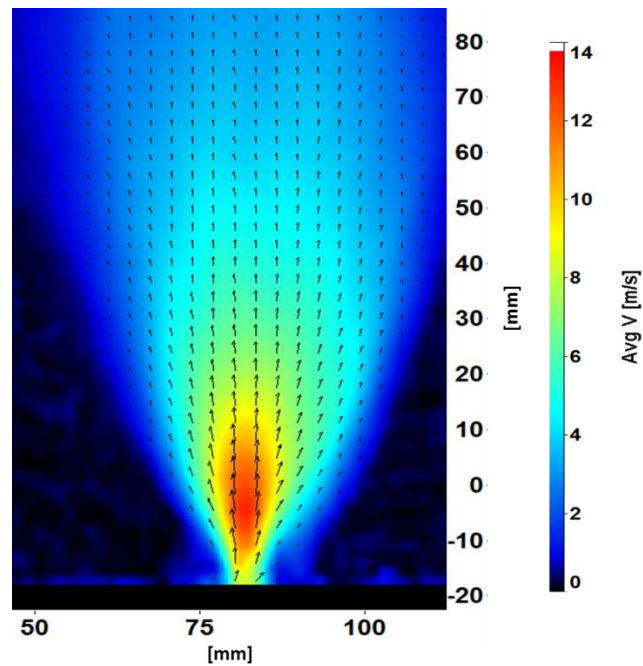


Figure 10 Average magnitude of velocity profile of synthetic jet actuator array configuration shown in Figure 9.

2.3 Wind Tunnel Experimental Setup

2.3.1 Backward Facing Step Model

The experimental apparatus used to conduct the experiments is shown in Figure 11 and consists of two aluminum 1" profile 80/20 frames with a cut out in the center. The entire top of the frame is covered with a piece of plastic with a similar center cut out shown in Figure 11. Both frames were designed to accommodate the actuators and allow for future modifications for testing different step heights. The center cut out in the plastic is shown close up in Figure 12. The cut out dimensions of the frames is 0.064m while the plastic slot is 0.089m. This allowed a lip of 0.0127m wide on each side for the static pressure plates and the actuators to sit on the lip; a close up of the center cut out with the actuator and static pressure ports is illustrated in Figure 12. The length of the cut out on Frame 1 is 0.203m which allowed for the actuator to move as far upstream as 0.193m. The length of the cut out on frame 2 is 0.254m which allowed for the actuator downstream of the step to be moved a maximum distance of 0.244m. To maintain the 2-D dimensionality of the flow, the ramp and platform spanned the entire width of the test section.

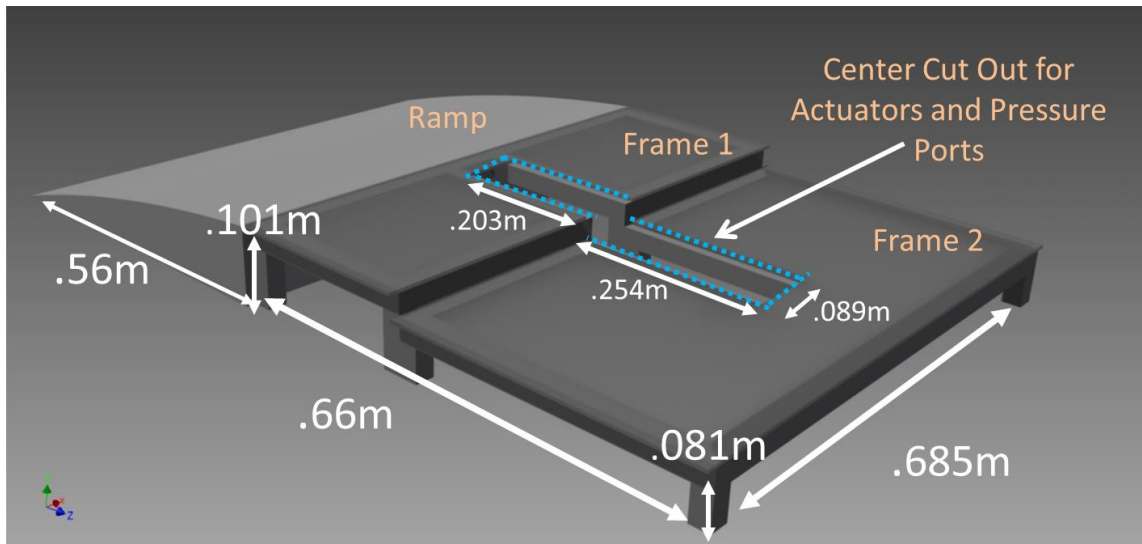


Figure 11 3D CAD model of step with dimensions

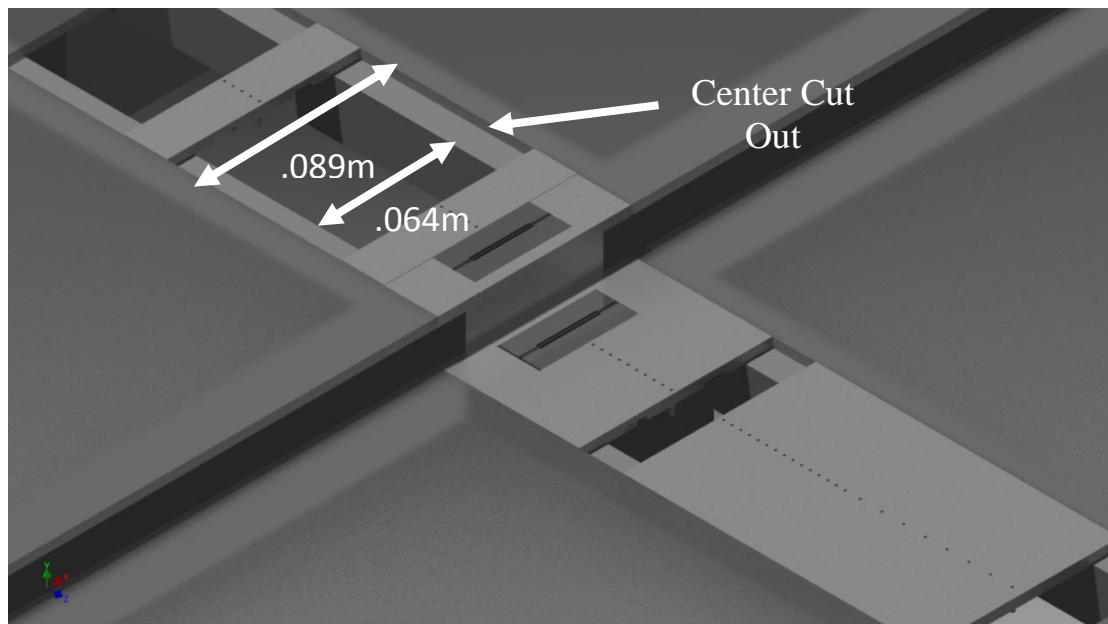


Figure 12 Close up of 3D CAD model center cut out with dimensions

2.3.2 Wind Tunnel Setup

The experiments were conducted in an Aerolab open circuit low speed wind tunnel at the University of Maryland. The wind tunnel has a test section of 0.71m x 0.5m x 1.2m and is capable of velocities spanning 0-60m/s. The floor of the test

section was modified with an external ramp, described in the previous section, to create a step geometry inside of the test section. Figure 14a-b shows a 3-D model of the test section setup. The synthetic jet actuators placed along the centerline of the tunnel are illustrated in Figure 14b. SJA1, as illustrated in Figure 13, refers to the upstream actuator located before the step and SJA2 refers to the downstream actuator. The two high speed cameras and pressure ports pictured in Figure 13 are described in further detail in a later section.

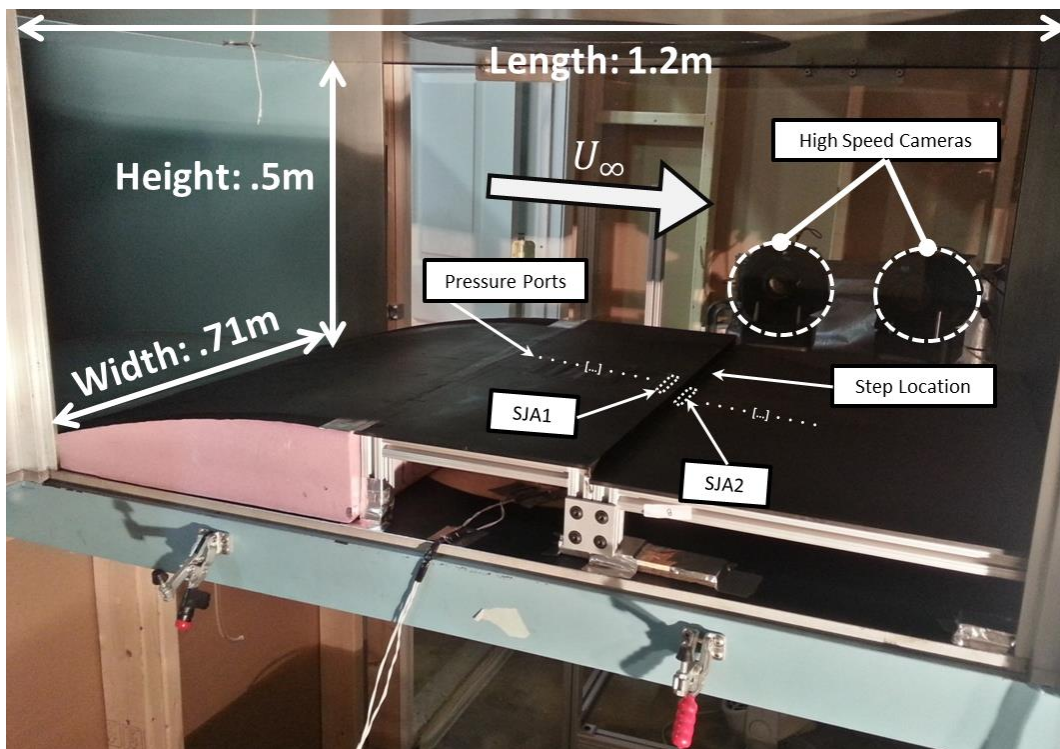


Figure 13 Photograph of experimental setup installed inside the test section of the wind tunnel. High speed camera location and actuator locations are denoted in the above figure

2.4 Overview of Experimental Test 1: Single Actuator Upstream

2.4.1 Overview of Test

The first set of tests consisted of using SJA1 to study the effect of actuator location with respect to the step and its influence on the resulting separation bubble. The step height for these tests was set to 14mm and the cross flow velocity was 8.75m/s, which corresponds to a $Re_h \approx 7800$ where Re_h is defined as:

$$Re_h = \frac{U_\infty h}{\nu}$$

where h is the step height, U_∞ is the cross flow velocity and ν is the kinematic viscosity of air, $\nu = 15.68 \times 10^{-6} \text{ m}^2/\text{s}$. The actuation frequency of the jets was kept constant at 1750Hz with a drive voltage of 108V.

The actuation frequency of the jets needs to be at least an order of magnitude higher than the natural frequency $St_{act} \sim O(10St_s)$ of the flow. This is briefly verified here and will be later discussed in Chapter 3 in more detail. A typical value of the Strouhal number for a backward facing step flow where the characteristic length is taken to be the step height is $St_s \approx 0.185$. Solving for the Strouhal number for the actuator yields the following:

$$St_{act} = \frac{f_{act} h}{U_\infty} \rightarrow \frac{1750\text{Hz} * .014\text{m}}{8.75\text{m/s}}$$

$$St_{act} = 2.8$$

Estimation for the shedding frequency of the step:

$$f \approx \frac{St_s U_\infty}{h} \rightarrow \frac{0.185 * 8.75\text{m/s}}{0.014\text{m}}$$

$$f \approx 115.6\text{Hz}.$$

Based on the above result, it was determined that the Strouhal number of the actuator is at least an order of magnitude higher than the natural frequency of the flow, or $St_{act} \sim O(10St_s)$.

2.4.2 Stereoscopic PIV Setup

Stereoscopic PIV measurements were taken to obtain quantitative measurements of the flow field and in particular to measure the effect of the actuator on the separation bubble and shear layer at the step. Two 1MPx Phantom V311 high speed cameras with a resolution of 1280 x 800 px and a Litron LDY300 ND:YLF laser were used to capture the stereo PIV images. Figure 13 is a photograph of the test setup in the wind tunnel. A laser sheet was oriented along the centerline of the actuators. In order to position the laser sheet inside the test section, a series of 4 mirrors were used to orient the laser sheet above the tunnel and into the test section as illustrated in Figure 15. The flow was seeded using mineral oil and a TSI 6 jet atomizer.

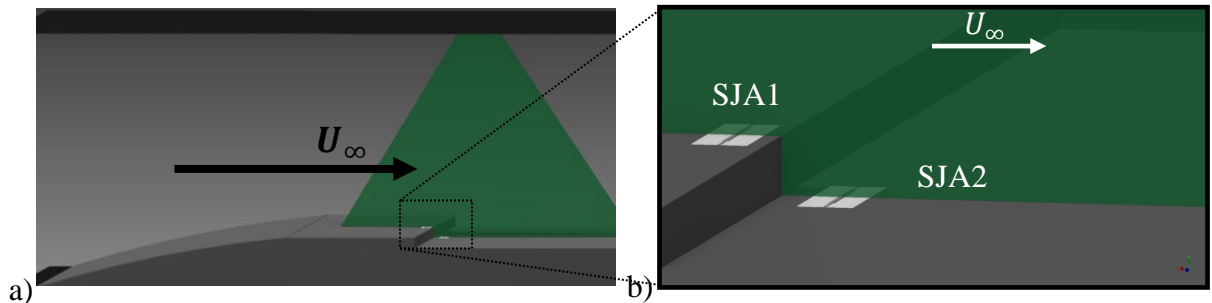


Figure 14 Experimental setup inside of the wind tunnel with laser sheet. (b) Enlarged view of actuator location before and after step.

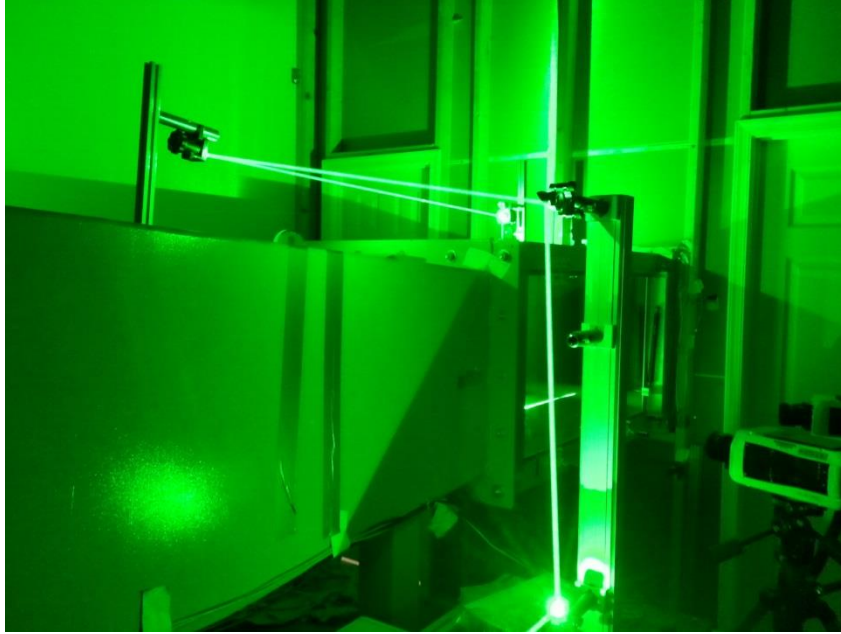


Figure 15 Photograph of experimental laser test setup

2.4.4 Details of Processing

Double frame PIV images were captured at 1750Hz. This was equal to the operating frequency of the synthetic jet actuators. For each test, 525 image pairs were captured by each camera and processed using the DaVis 8.1 software suite by Lavisision Inc. A stereo cross-correlation was used with a multi-pass interrogation window size of 32 x 32 down to a window of 16x16 with a 50% overlap on each pass. A median filter was applied using universal outlier detection for post processing purposes using the DaVis software. All of the PIV data presented in this paper represents time averaged results.

2.5 Overview of Experimental Test 2: Actuator Upstream and Downstream of Backward Facing Step

2.5.1 Overview of Test and Parameters

The second set of tests investigated the interaction between the separated flow over the step and the two actuators, SJA1 and SJA2. The step height for this set of tests was increased to test SJA2 at a point $<1h$; because of actuator dimensions, this was not possible with the previous step height. For this study, the free stream velocity was held constant at 7.2m/s, which corresponds to a freestream Reynolds number of $Re_h \approx 9000$. The actuators were operated at a constant frequency of 1500Hz. It is important to note that this frequency differs slightly from the previous test. This was done in order to mitigate the risk of damaging the piezoelectric disks during tests by operating at or close to resonance. The disks were driven at voltages between 40V-120V.

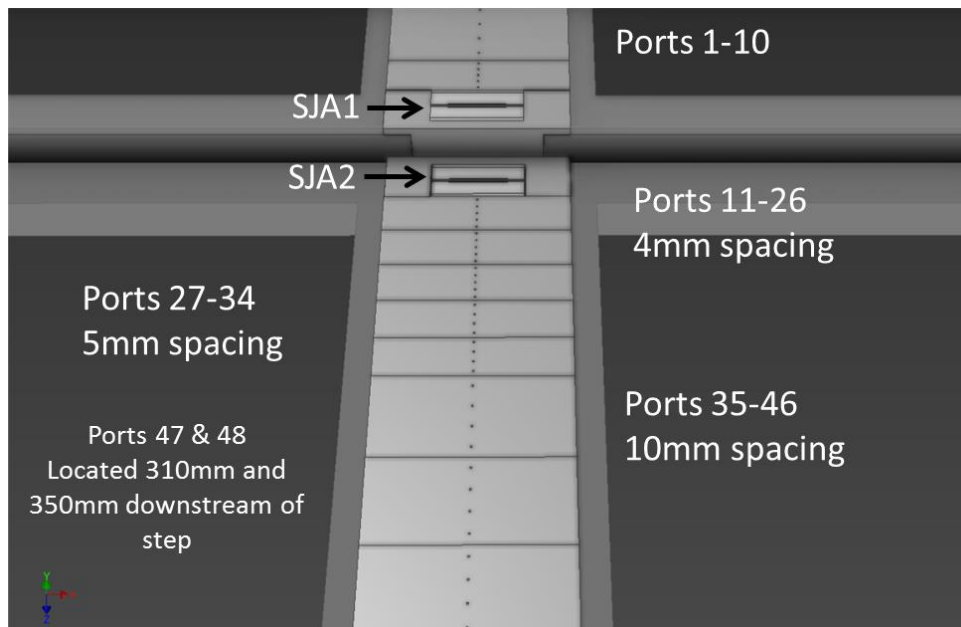


Figure 16 Step model with layout of static pressure ports along bottom wall

The step model was outfitted with 48-static pressure ports, along its center-line as shown in the pressure port arrangement illustrated in Figure 16.

The first ten ports were placed upstream of the SJA1 in order to reference upstream conditions. The remainder of the ports were located downstream of the step as far as 350mm or 17.5h.

The two parameters of interest were the distance of SJA2 from the step and the momentum coefficient of each jet, $C_{\mu 1}$ & $C_{\mu 2}$. As the location of SJA2 was moved downstream, it was necessary to alter the locations of the pressure ports surrounding it. Thus a simple, easily maneuverable method was necessary to complete the setup for each subsequent change of location of SJA2. A set of plastic plates dimensioned to match the width of the actuator were used with the pressure ports printed along the center line.

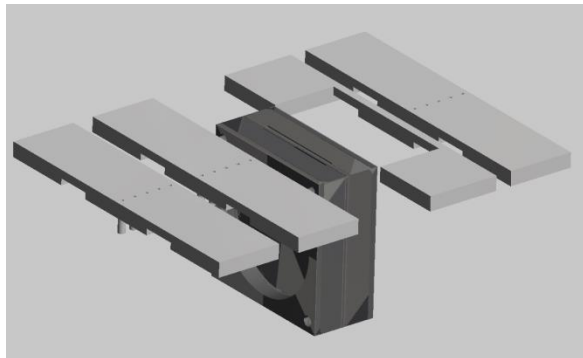


Figure 17 3-D CAD model of plastic pressure port plates illustrated with synthetic jet actuator

The first location of SJA2, the actuator was located between 0-1h and the first plastic plate was located between 1h-2h. As the actuator was moved downstream h, the first plastic plate was moved to 0-1h while the actuator is between 1h-2h. Figure 17

contains a 3-D CAD model of the actuators and plastic inserts. The plastic pressure port inserts were printed using an Objet Eden 350V polyjet rapid prototype printer with layer resolution of $16\mu\text{m}$.

2.5.2 Pressure measurement details

The tests were conducted using a 48-channel scanivalve with a Sensor-Technics differential low pressure sensor that has a range of 0-50 Pa. The data was acquired using a National Instruments data acquisition unit NI-USB 6251. To obtain sufficient time averaged pressure measurements, 1000 samples were acquired over 10 seconds for each port. A Labview program was written for this test to provide the actuation signals to the amplifiers and to control the stepping motor on the scanivalve.

2.6 Computational Study of Flow Over Backward Facing Step

A 2-D CFD study was initiated to simulate the experimental tests with flow over a backward facing step and SJA without actuation. The flow over a backward facing step is one of the most widely studied flow phenomena in CFD. A baseline CFD study was modeled in order to compare the experimental baseline with a numerical model using commercial software, Comsol Multiphysics. A 2-D steady state analysis was conducted using Reynolds Averaged Navier-Stokes with a $k-\varepsilon$ turbulence model. The upstream and downstream boundary conditions were taken from the experimental data. The model in the computational domain used the same dimensions as the experimental model. The dimensions and boundary conditions are shown in Figure 18. The inlet velocity profile was obtained using an additional model that is not shown below to allow for the velocity profile to fully develop to the

specified value. The external model was dimensioned to be the same height and 100 times the length of the one shown below in Figure 18. The outlet boundary was specified to match the experimentally recorded downstream pressure which was recorded to be -23.5Pa. The walls were modeled with a no slip condition.

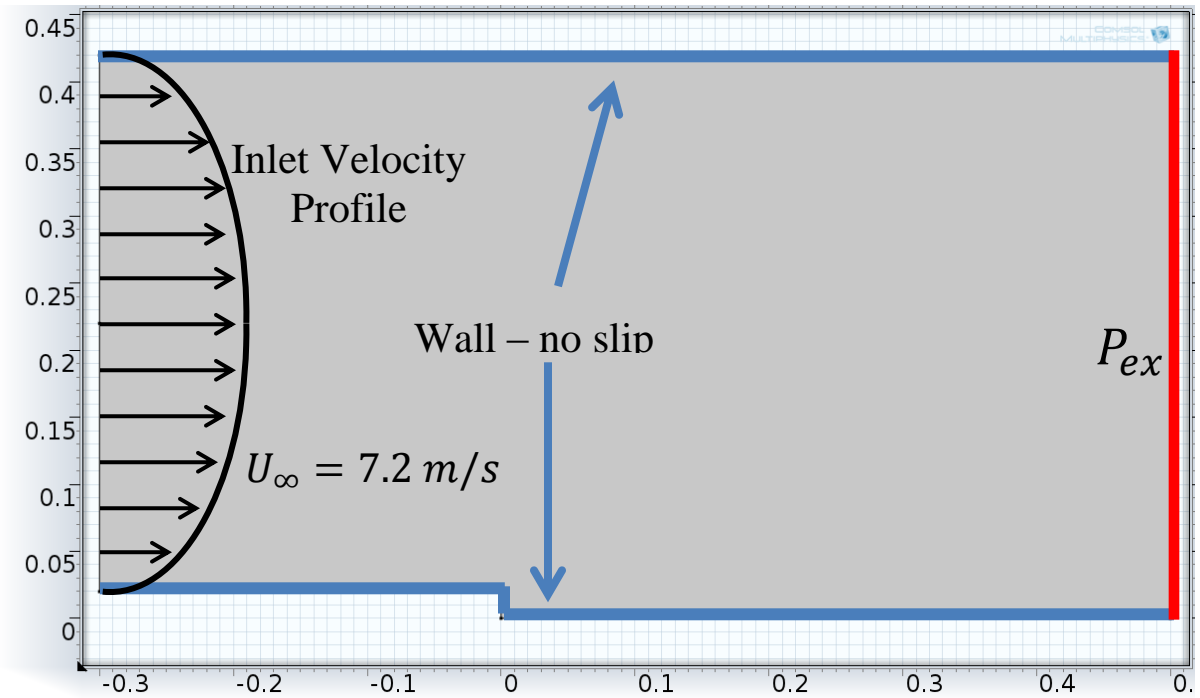


Figure 18 Illustration of computational model with boundary conditions

Chapter 3: Results of Experimental Test 1: Single Actuator

Upstream

3.1 Backward Facing Step with Single Actuator Upstream

The output velocity of SJA1 was measured before and after the tests using stereoscopic PIV to ensure that the actuator output remained constant throughout the testing. The averaged velocity profile of the actuator used in the tests can be seen in Figure 19, with an average peak velocity of 13m/s. Two non-dimensional parameters are often used to assess the synthetic jet actuator strength. These are velocity ratio and momentum coefficient. The velocity ratio, VR , is the ratio of the average peak jet velocity of the actuator to the free stream velocity and is defined as:

$$VR = \frac{U_j}{U_\infty}$$

where U_j is the average peak velocity of the jets and U_∞ is the freestream velocity.

The velocity ratio for this test was kept constant and chosen to be $VR \approx 1.5$.

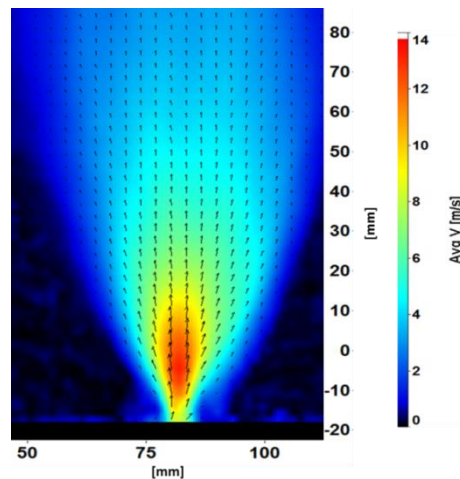


Figure 19 Average magnitude of velocity profile of synthetic jet actuators

The momentum coefficient, C_μ , is the ratio of ejected momentum from the synthetic jet actuator to the total flow momentum. The momentum coefficient C_μ , can be defined as:

$$C_\mu = \frac{2\rho_j U_j^2 b}{\rho U_\infty^2 c}$$

where ρ and ρ_j are the freestream and jet fluid densities, b is the orifice width of the actuators, U_j is the average peak velocity of the jets, U_∞ the cross flow velocity, and c a characteristic length (Ugrina 2007). For these experiments, the characteristic length was set equal to h . The density for the current application of synthetic jet actuators in air is constant so the momentum coefficient can be further simplified to:

$$C_\mu = \frac{2U_j^2 b}{U_\infty^2 h}$$

The momentum coefficient was kept constant at $C_\mu = .31$.

3.2 Actuator Location

The location of SJA1 upstream of the step was varied from 1.07h – 7.14h (15mm-100mm). Four different distances from the step were tested: 15mm \pm 0.5mm (1.04h \pm 0.025h), 30mm \pm 0.5mm (2.14h \pm 0.025h), 60mm \pm 0.5mm (4.28h \pm 0.025h), and 100mm \pm 0.5mm (7.14h \pm 0.025h) which are illustrated below in Figure 20. The distance measured is from the center of the actuator to the step edge.

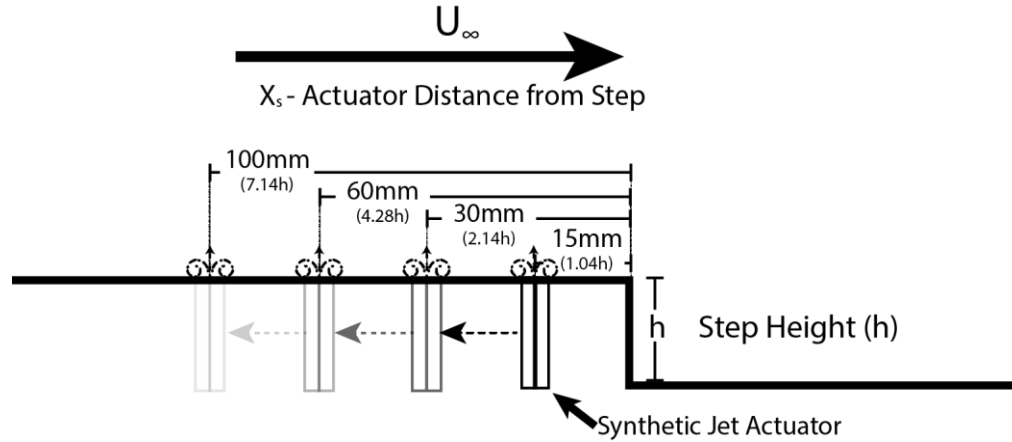


Figure 20 Illustration of experimental test parameters for experimental test 1 with specified dimensions

The free stream velocity was measured using stereoscopic PIV results. To calculate the freestream velocity from the PIV results, a region before the step where the velocity was uniform was chosen and an average velocity was calculated from that region. This is illustrated in Figure 21.

3.3 Boundary Layer State Before Separation

The boundary layer state before the flow separates is important to evaluate as the separation length can vary depending on if the boundary layer flow is laminar or turbulent. Additionally, the boundary layer height and state are important to assess in order to compare this work with others.

The boundary layer height before separation was measured using the time averaged velocity field generated from the stereoscopic PIV results for the baseline case without actuation. The boundary layer height was assessed over a small region upstream of the step by finding the crossflow velocity vector $U(y)_{bl} = 0.99U_{\infty} \pm 0.25\% * U_{\infty}$. This can be better stated as:

$$0.8975U_{\infty} \leq U(y)_{bl} \leq 0.9925U_{\infty}.$$

The boundary layer height was found to be approximately $\delta \approx 11.1\text{mm}$. The boundary layer thickness can then be normalized with respect to the step height, which yields, $\delta \approx 0.79h$.

According to classical laminar boundary layer theory, the boundary layer thickness for flow over a flat plate is approximately:

$$\delta \approx 5.2\sqrt{x^2/Re_x}$$

where x is the distance downstream from the start of the boundary layer, Re_x is the Reynolds Number based on this distance (Barlow et al.). An estimate of the x distance was used based on the distance from the start of the contraction in the inlet to the step which is approximately 2.91m. Using this value and the above theory, the boundary layer thickness was calculated to be $\delta \approx 11.2\text{mm}$. However, it is fair to note that this calculated value might be misleading since the flow travels through two contraction sections before reaching the step and these contraction sections will decrease the boundary layer thickness. Instead, the boundary layer could be turbulent for which the equation for the boundary layer thickness over a flat plate is given by (Barlow et al.):

$$\delta \approx .37x/Re_x^{1/5}$$

Evaluating the boundary layer thickness for a turbulent flow with the same values used as before yields, $\delta \approx 63.7\text{mm}$. This is much larger than the measured value; however, this represents a turbulent boundary layer development over a flat plate that is 2.91m in length when in reality the tunnel is not a flat plate as there are again two contraction sections located before this x location. The reality is that

both estimations are false; even though the laminar boundary layer calculation gave a good estimation of the actual measured boundary layer, it does not take into account these specifications. Furthermore, most boundary layer flow inside wind tunnels are known to be turbulent so this is again another reason why the laminar boundary layer approximation does not fit (Barlow et al). Therefore, the more likely scenario is that the boundary layer is turbulent and that it is difficult to numerically estimate this with either of the above two equations. Consequently, the results presented below for the reattachment length, X_R represent the case where the boundary layer flow upstream of separation is turbulent.

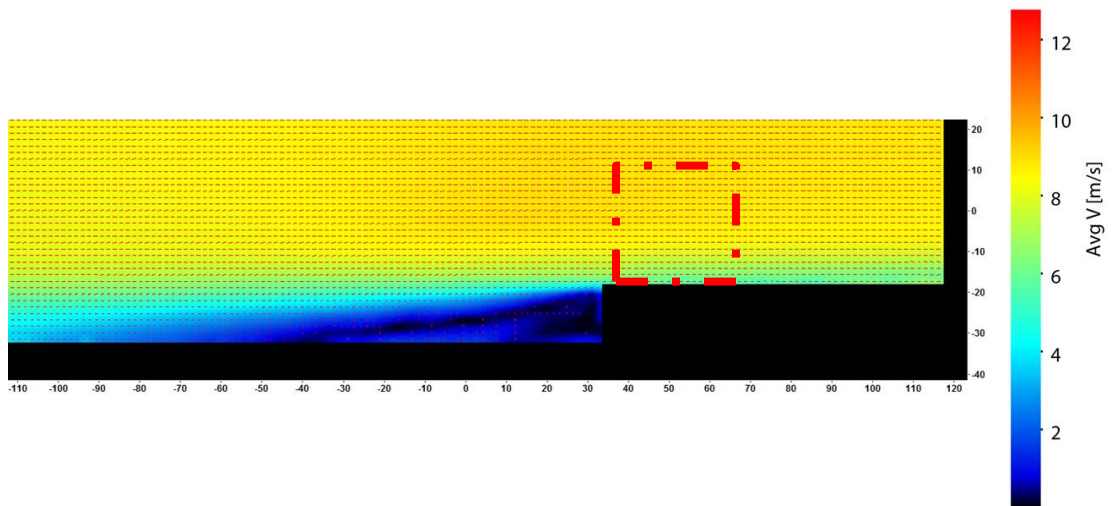


Figure 21 Time averaged experimental PIV results for flow over backward facing step without synthetic jet actuation. Red box indicates region used to assess the boundary layer height

3.4 Assessing Reattachment: Forward Flow Probability

The location of flow reattachment is time dependent. For this reason, a statistical method (the Forward Flow Probability or FFP) was used to assess the mean point of reattachment. The forward flow probability is a measure of how often a

vector is facing downstream versus upstream. For results obtained using PIV, it can be defined as:

$$FFP = \frac{1}{N} \sum_1^N \frac{u}{|u|}$$

where N represents the number of instantaneous vector fields evaluated throughout and u is the x-component of the velocity vector along the bottom wall. The y-component is not of importance as the direction of x-component can be assessed independently of the vertical component. $FFP=1$ indicated velocity vectors facing downstream 100% and $FFP=0$ indicated velocity vectors facing downstream 0%, or reversed flow. It can also be considered as a method to assess the unsteadiness of the x-component of velocity. In order to determine the reattachment point, it was desirable to evaluate the location of mean reattachment which represents the second point along the bottom wall where $FFP=0.5$. Note that for flow over a backward facing step there are often two locations along the wall for which $FFP=0.5$. The first location is the point that separates the primary and secondary recirculation regions and the second location is the point of mean reattachment.

3.5 Length of Separated Flow Over Backward Facing Step

Before discussing the results of the test cases with the actuators on, the baseline flow, without any actuation, was examined a little further. Using the forward flow probability for the baseline flow, the separation length was found to be approximately 5.8h. This experimental finding is consistent with prior work that reports the mean reattachment length is typically between 5h-7.5h, depending on the Reynolds Number (Rajasekaran, Spiazzi et al. 2002). This confirms that the value

obtained using the forward flow probability yields results that are consistent with other published works. As an additional means of verification, a numerical simulation was performed. The results from the numerical model are shown below in Figure 22. The recirculation length obtained numerically from the model is 5.88. The percent difference between the experimental and numerical model 1.3% which is small and provides an additional method to verify the fidelity of the output produced with the forward flow probability.

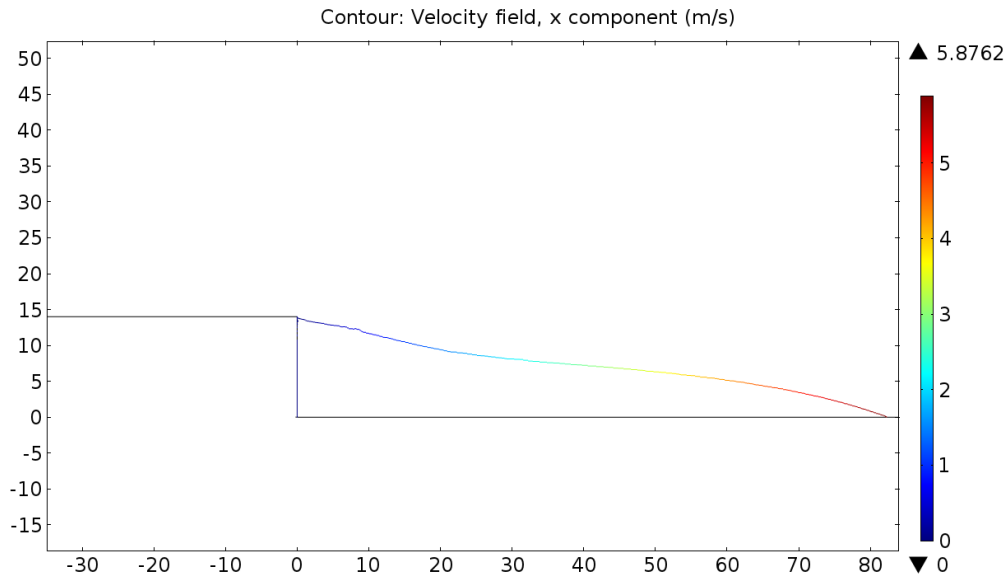


Figure 22 Computational results for flow over a backward facing step illustrating length of separation bubble

3.6 Strouhal Number of Flow Over a Backward Facing Step

One of the objectives of this research was to study ‘the effects of synthetic jet actuators on the flow over a backward facing step at forcing frequencies which are an order of magnitude higher than the natural frequency $St_{act} \sim O(10St_s)$ ’. For flow over a backward facing step, two typically accepted values for the Strouhal are, $St_s \approx 1$ when the characteristic length is taken to be X_R , and $St_s \approx 0.185$ when the

characteristic length is taken to be the step height. This was briefly addressed in Chapter 2, Section 2.4.1 where the Strouhal number was calculated with the step height as the characteristic length scale. The Strouhal number is again calculated, but here, the characteristic length scale is taken to be the experimental reattachment length, X_R , introduced above. The Strouhal number for the actuator is calculated as follows:

$$St_{act} = \frac{fX_R}{U_\infty} \rightarrow \frac{1750 * (5.8 * .014m)}{8.75m/s}$$

$$St_{act} = 16.24$$

Estimation for the shedding frequency off the step:

$$f \approx \frac{St_s U_\infty}{X_R} \rightarrow \frac{1 * 8.75m/s}{(5.8 * .014m)}$$

$$f \approx 107.7Hz.$$

The value for f calculated above is very close to the one calculated in Chapter 2, which was $f = 115.6Hz$, which is less than a 10% difference between the two. More importantly, the above calculation further validates the Strouhal number for the actuator to be at least an order of magnitude larger than the Strouhal number of the flow.

3.7 Time-Averaged PIV Results

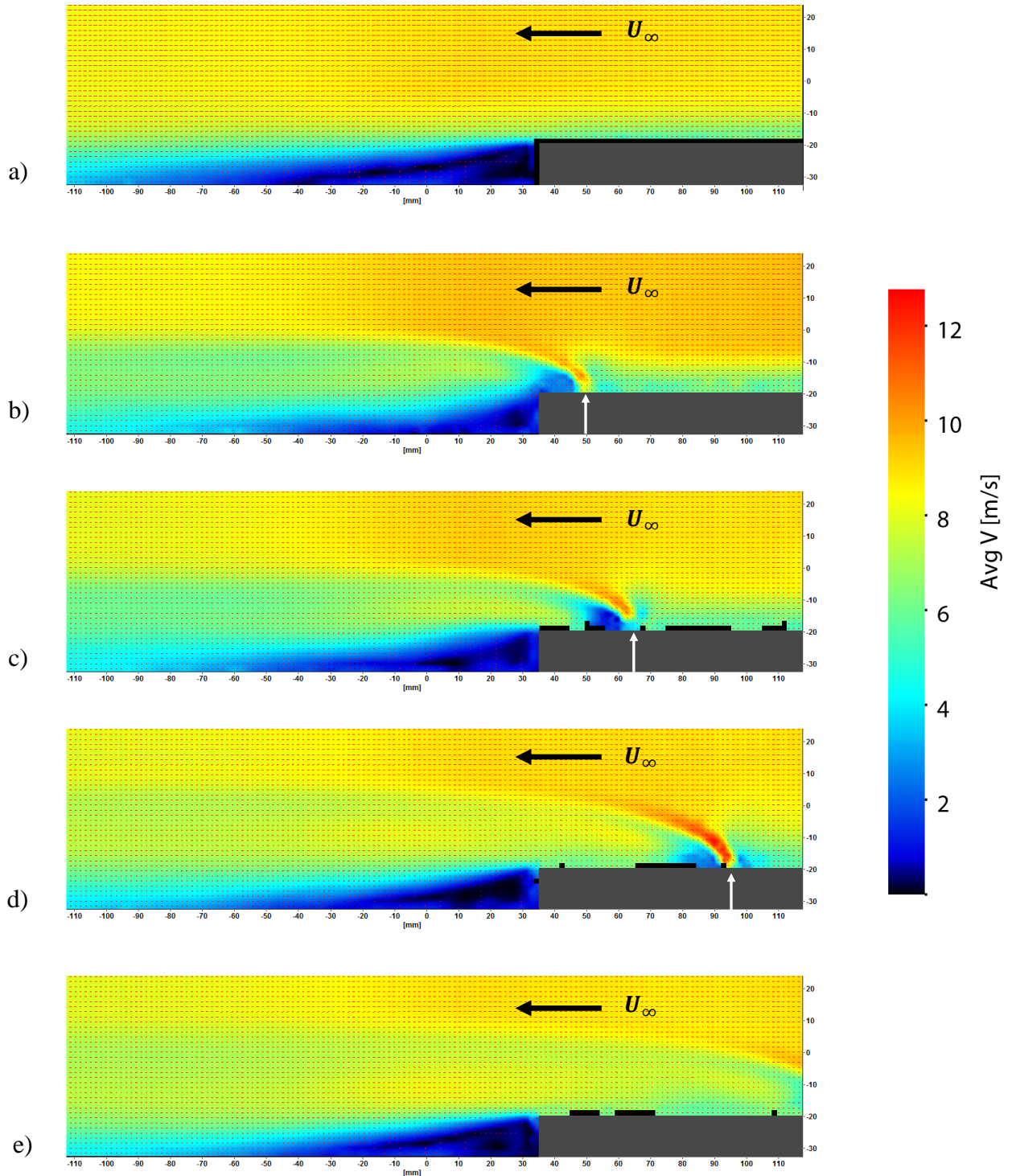
The time averaged PIV results are presented below in Figures 23a-e. Note the blacked areas in these Figures correspond to masked areas where there was a strong reflection in the PIV images from the step and the grey rectangle corresponds to the

floor of the tunnel. The actuator placed $1.07h$ upstream, as well as the drastic effect of the actuator on the recirculation length step can be clearly seen in Figure 23b. Immediately downstream of the actuator there is a small recirculation region located at the edge of the step which alters the streamwise pressure gradient, pulling the boundary layer down towards the floor and promoting mixing of the shear layer. In Figure 23c-e the actuator is moved further upstream and the effect is slightly diminished; however, there is still a noticeable reduction. This can be attributed to the increase in turbulence upstream of the step as a result of the actuators being located there.

It is worthwhile to discuss this single actuator case in a little more in depth as it provides insight into the overall fluid physics of this study. From Figure 23b, the jet core can be seen clearly as the trajectory of the jet is turned into the crossflow, essentially creating a virtual shape change through the displacement of the local streamlines. There is also a change in the streamwise pressure gradient which has implications towards flow separation. This modification of the streamwise pressure gradient upstream of separation using synthetic jets has been shown by others to delay or suppress separation (Honohan 2000, Glezer et al 2003). From Figure 23b it can be seen that the flow is pulled down towards the step in a shorter distance essentially causing a reduction in the separation length. Analyzing the results that are summarized in Table 1, the effect of the actuator closest to the step is almost twice the effect of the other actuator locations. It is notable that actuation as far upstream as $7.14h$ is still felt at the step.

Table 1: Reduction in Separation Length for Different Values of SJA1 location, X_R

	Baseline	$X_s=1.07h$	$X_s=2.14h$	$X_s=4.28h$	$X_s=7.14h$
Separation Length	5.8h	2.6h	4.1h	4.2h	4.4h
Percent change in separation length	N/A	55 %	29%	28%	24%



Chapter 4: Results of Experimental Test 2: Actuator upstream and downstream

4.1 Scaling of F^+

The second experimental test involved the use of two actuators. SJA1 was located upstream from the step, and SJA2 was located downstream from the step. The actuator location closest to the step had the largest influence on the region of separated flow. For this study, the upstream actuator was kept constant at 15mm \pm 0.5mm upstream from the step, or $0.75h \pm 0.025h$. For the current study, the cross flow velocity, actuation frequency and step height differ from the study that was presented in Chapter 3.

It can be shown that the change in crossflow velocity, U_∞ and actuation frequency, f_{act} do not have an effect on the scaling of the physics by using the non-dimensional frequency, F^+ . The non-dimensional frequency, F^+ is defined as:

$$F^+ = \frac{f_{act}L}{U_\infty}$$

where f_{act} is the actuation frequency of the synthetic jet actuators, L is a physical reference length which for this setup is taken to be the distance from SJA1 to the step edge and U_∞ is the cross flow velocity.

The actuation frequency, f_{act} was kept constant at 1750Hz, the first actuator location upstream of the step, X_s was set to 15mm, and the cross flow velocity was 8.75m/s. Solving for F^+ :

$$F^+ = \frac{1750\text{Hz} * 0.015\text{m}}{8.75\text{m/s}}$$

$$F^+ = 3$$

The location of SJA1 remained 15mm, and the cross flow velocity was 7.2m/s yields the following:

$$F^+ = \frac{1500\text{Hz} * 0.015\text{m}}{7.2\text{m/s}}$$

$$F^+ = 3.125$$

It is apparent that for the two different experiments, even though the frequencies and cross flow velocities differ, the non-dimensional frequency of SJA1 essentially remains the same, which means the physics were scaled appropriately for the upstream actuator.

4.2 Location of SJA2

The step height was increased to 20mm from 14mm to be able to test the downstream actuator, SJA2, at a location $X_{SD} < 1h$. It was shown in experimental test 1 that for the single actuator located 7.14h upstream of the step, which performed the least effectively, the separation length was still reduced 25% to 4.4h. Using this result, it was decided to bound the testing location of the downstream actuator, SJA2, to $X_{SD} < 5h$. This was done in order to keep SJA2 inside a region of the flow influenced by the upstream actuator, SJA1. For the actual experimental setup, the location of SJA2 downstream of the step, X_{SD} , was varied in increments of ~20mm

from .75h – 4.63h (15mm – 92.5mm). The different locations of SJA2, X_{SD} , and the location of SJA1 are illustrated below in Figure 24.

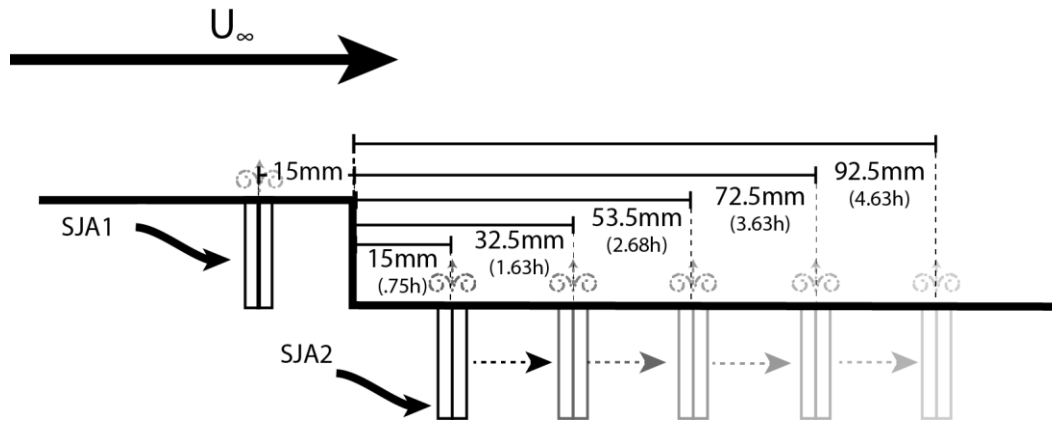


Figure 24 Illustration of experimental test parameters for second study with dimensioned actuator locations

4.3 Momentum Coefficient $C_{\mu 1}$ & $C_{\mu 2}$

The momentum coefficients, $C_{\mu 1}$ & $C_{\mu 2}$ of SJA1 and SJA2, were also varied. The previous study looked at the influence of location of SJA1, X_S , on affecting the separation length. The majority of the jet flow from SJA1 was directed upwards above the step and outside the boundary layer. It was determined that the momentum coefficient of SJA1 was too large to achieve any noticeable interaction between an actuator located downstream inside the wake. For this study, three momentum coefficients for SJA1 were tested,

$C_{\mu 1} = [0.02, 0.057, 0.094]$. Four momentum coefficients for SJA2 were also tested,

$C_{\mu 2} = [0, 0.043, 0.064, 0.088]$.

4.4 Computational Results of Flow Over a Backward Facing Step

The results from the 2-D numerical simulation of flow over a backward facing step without actuation are presented below in **Error! Reference source not found.**. The experimental baseline has been plotted alongside the simulation results for comparison. The numerical and experimental results presented in **Error! Reference source not found.** illustrate the variation in the pressure coefficient, C_p , along the non-dimensionalized x axis, from the step edge to 8.5h downstream. The pressure coefficient, C_p is defined as:

$$C_p = \frac{(p - p_{ref})}{0.5\rho U_\infty^2}$$

where p_{ref} here was chosen based on an average value obtained from the upstream pressure data.

The numerical model generally shows good agreement with the experimental data. However, the numerical model under predicted the pressure directly after the step. The numerical model also under predicted the minimum value that occurs in the experimental baseline at $x/h=2.5$. Overall, the numerical model performed well in its ability to capture the profile of the curve as well as, to a high degree, the physical values that are represented in the experimental data presented below.

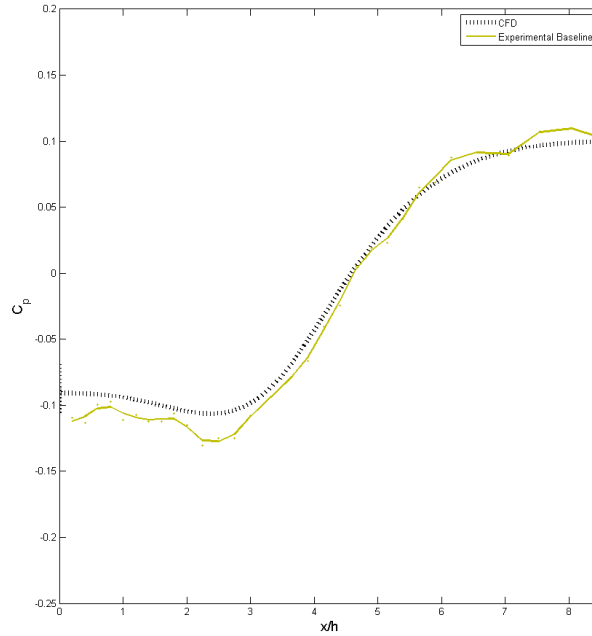


Figure 25 Pressure coefficient downstream of backward facing step from numerical results (dashed line) and experimental results (solid line)

4.5 Three Regions

Examining the numerical and experimental results in **Error! Reference source not found**, three distinct regions are identified to partition the trends in the pressure coefficient as illustrated in Figure 26. These three regions were designated as, I, II, and III and are shown in the plot below represent three different phenomenological regions in the flow. The three regions defined as follows: Region I spans from 0 – 2.5h, Region II from 2.5h – 6h, and Region III from 6h – 8.5h. In Chapter 1, the flow over a backward facing step separated into three primary regions, the separated shear layer, the recirculation, and the reattachment zone. Region I from 0-2.5h represents the region where the separated shear layer begins to develop before it begins to curve down towards the step. Region II as shown in Figure 26 is from 2.5h

– 6h and can be characterized as the region where the pressure recovery occurs and as discussed earlier, the region of recirculation. Region III, from 6h – 8.5h illustrates the far field where the flow has reattached after the reattachment zone.

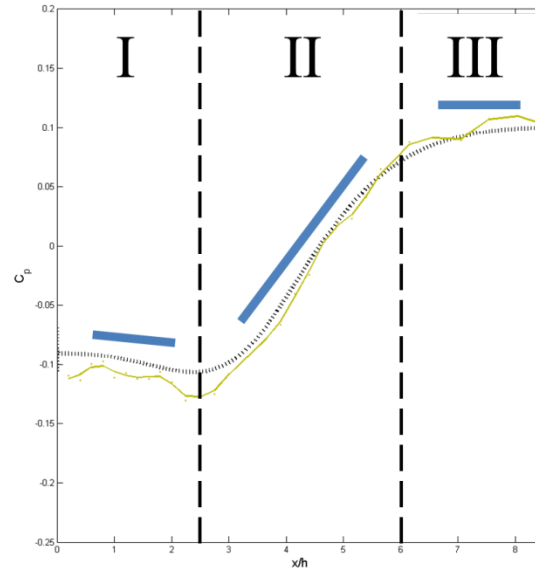


Figure 26 Illustration of the three different regions shown in the results of the pressure coefficient downstream of the step

4.6 Experimental Test 2 Results: Pressure Coefficient

The pressure coefficient results are presented in pairs of two for each of the different X_{SD} locations, highlighting the two most interesting values of $C_{\mu 1}$ tested. The momentum coefficient of SJA1, $C_{\mu 1}$ was tested at three different values; however, the results will focus on the two extremes, the smallest value tested, $C_{\mu 1} = .02$ and the largest value tested, $C_{\mu 1} = .094$ as shown below in Figure 27. The results for X_{SD} are only shown for 3 out of 5 of the locations as the other two represent the intermediate cases. The cases that will be presented below are as follows: $X_{SD} = .75h, X_{SD} =$

$2.68h$, & $X_{SD} = 4.63h$ which equate to the first location, the middle location, and the furthest downstream location.

Each of the figures contain two plots which correspond to the lowest (top plot) and highest (bottom plot) momentum coefficient of SJA1, $C_{\mu 1} = .02$ & $C_{\mu 1} = .094$, respectively. Note the location of the downstream actuator is denoted by a dashed red line and labeled SJA2; this is the center of the actuator and it spans $\pm .5h$ of this dashed line.

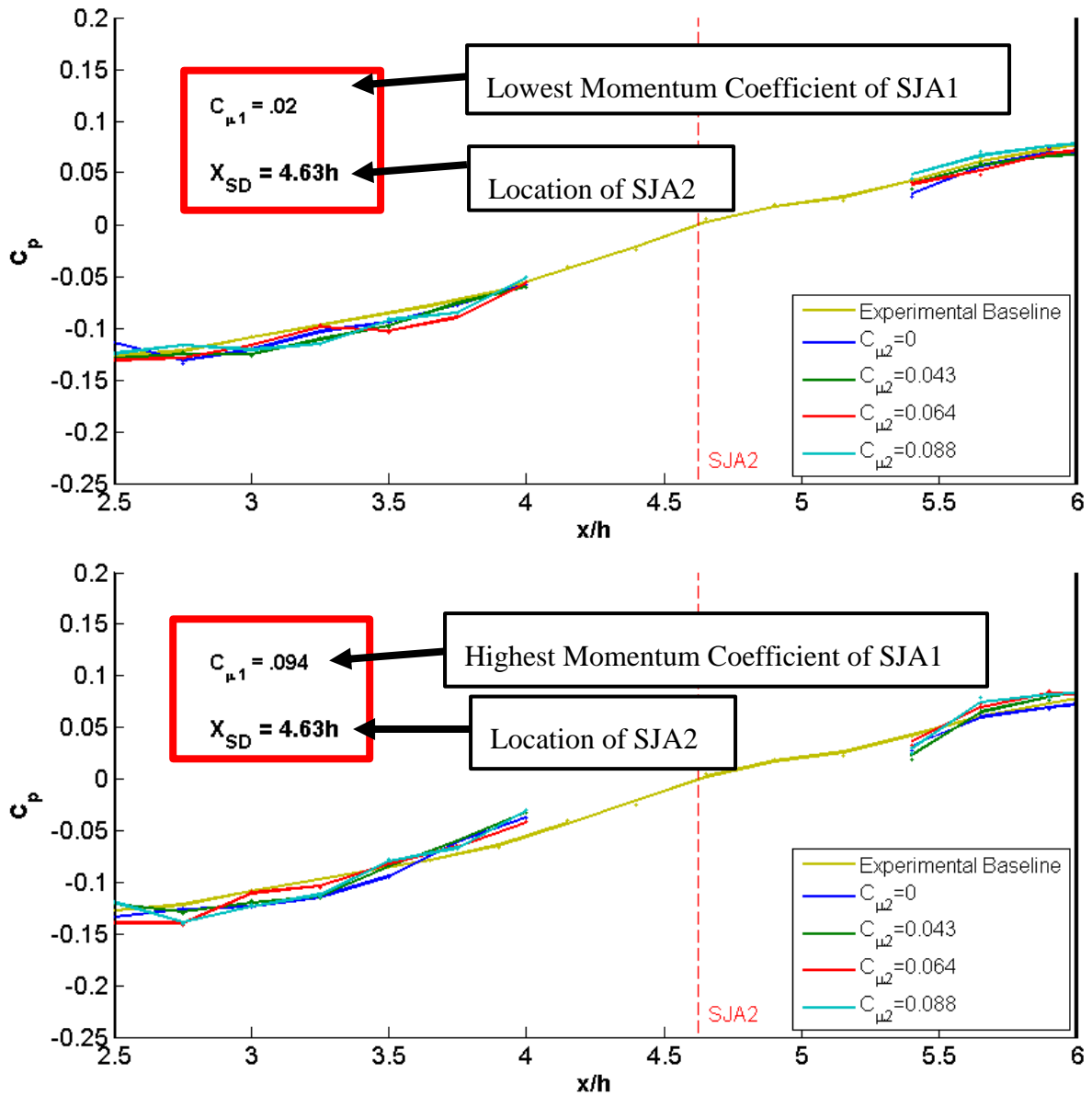


Figure 27 Format of results that will be presented (a) $C_{\mu 2}=0.02$ (b) $C_{\mu 2}=0.094$. for all three regions. (Only Region II shown above for illustration purposes)

4.7 Pressure Coefficient Results in Region III

The results from the time averaged pressure measurements are presented below in Figure 28 – 30 for $X_{SD} = .75h$, $X_{SD} = 2.68h$, and $X_{SD} = 4.63h$ respectively. Once again, Region III represents the far field flow in which reattachment of the baseline case flow over a backward facing step with actuation has occurred in the time-averaged flow field. Analyzing the results of Region III in Figure 28 – 30, there is very little discernible difference between all the different plots presented. This indicates that for all cases tested, C_p is invariant to both $C_{\mu 1}$ and $C_{\mu 2}$. The conclusion from this is that flow in Region III for all cases is considered statistically stationary.

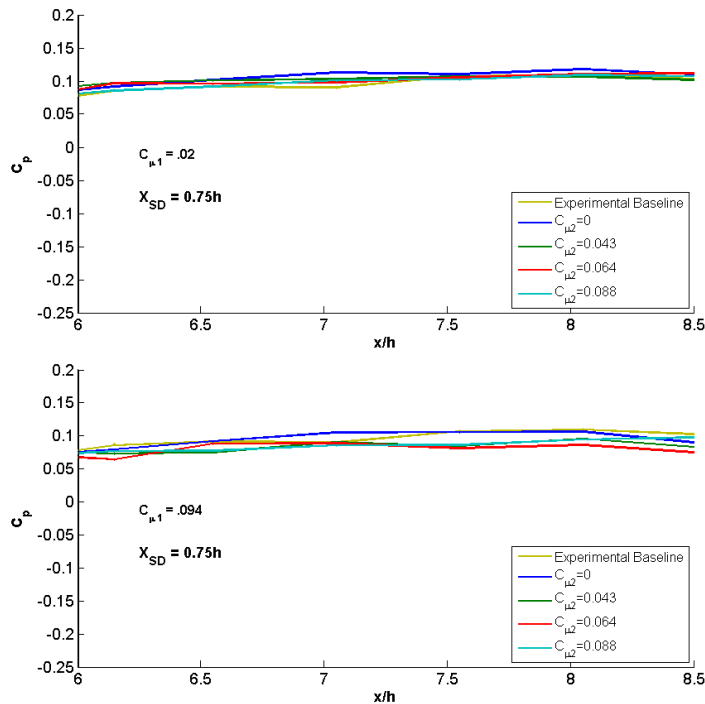


Figure 28 Region III $X_{SD} = .75h$ – Pressure coefficient downstream of step with varying momentum coefficient for SJA2, $C_{\mu 2}$. (a) Constant momentum coefficient for SJA1, $C_{\mu 2}=.02$ (b) Constant momentum coefficient for SJA1, $C_{\mu 2}=.094$.

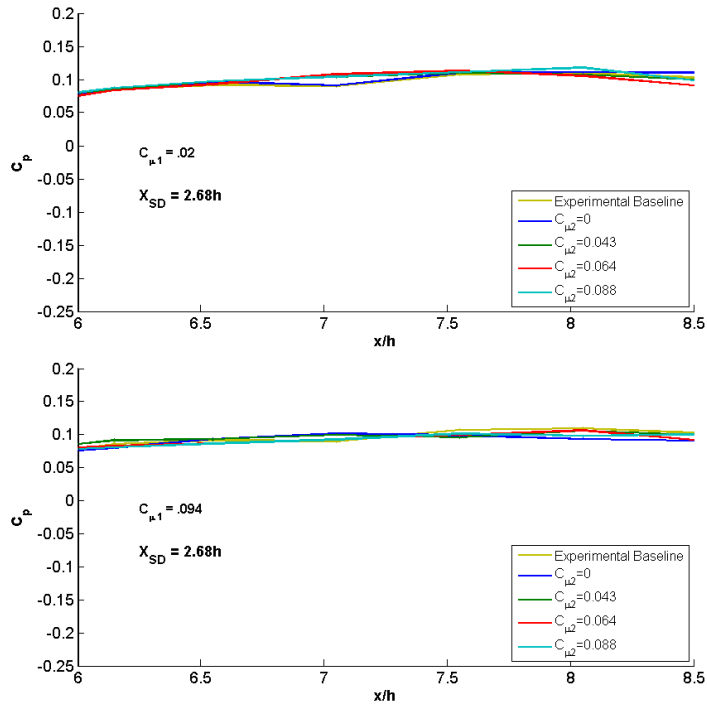


Figure 29: Region III $X_{SD} = 2.68h$ – Pressure coefficient downstream of step with varying momentum coefficient for SJA2, $C_{\mu 2}$. (a) Constant momentum coefficient for SJA1, $C_{\mu 2} = 0.02$ (b) Constant momentum coefficient for SJA1, $C_{\mu 2} = 0.094$.

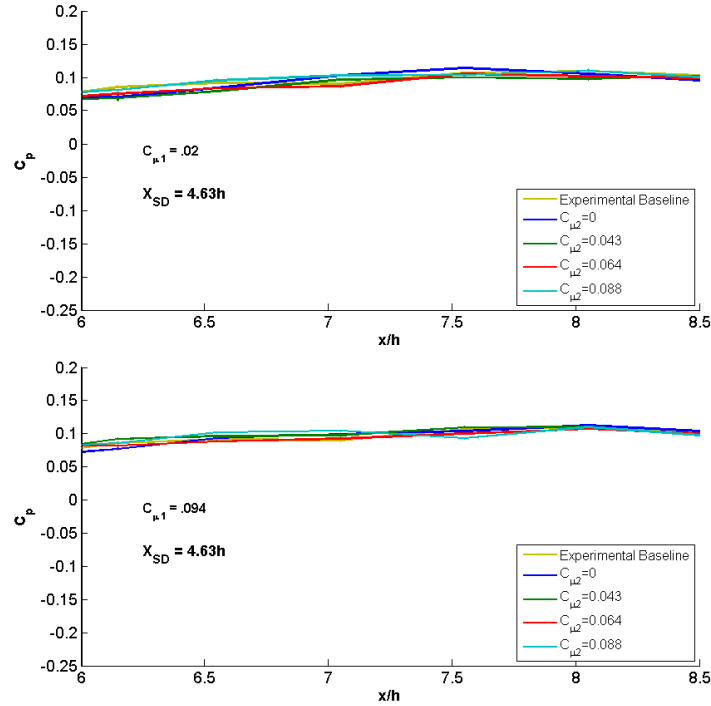


Figure 30: Region III $X_{SD} = 4.63h$ – Pressure coefficient downstream of step with varying momentum coefficient for SJA2, $C_{\mu 2}$. (a) Constant momentum coefficient for SJA1, $C_{\mu 2}=.02$ (b) Constant momentum coefficient for SJA1, $C_{\mu 2}=.094$.

4.7.1 First Order Approximation of $\frac{\partial C_p}{\partial x}$ in Region III

A first order approximation of $\frac{\partial C_p}{\partial x}$ was performed over the interval of 6.5h-8h to support the previous claim that C_p is invariant to both $C_{\mu 1}$ and $C_{\mu 2}$. The results from the first order approximation, shown below in **Error! Reference source not found.** – **Error! Reference source not found.**, are plotted against the momentum coefficient of SJA1, $C_{\mu 1}$, for the different values of $C_{\mu 2}$, the momentum coefficient of SJA2. By examining **Error! Reference source not found.** – **Error! Reference source not found.**, the approximated value of $\frac{\partial C_p}{\partial x}$ in all three figures does not differ much from the experimental baseline which is shown in the plots as a black dotted

line. Table 2 shows the calculated standard deviation of the approximated $\frac{\partial C_p}{\partial x}$ for each test case of $C_{\mu 1}$ and X_{SD} . The results shown in Table 2 reveal that for each value of C_{μ} , the standard deviation for the different values of X_{SD} do not vary much. This indicates again that for all cases tested, C_p is invariant to both $C_{\mu 1}$ and $C_{\mu 2}$ as for all the different test cases the values are close in value.

Table 2: Standard Deviation in 1st order Approximation of $\frac{\partial C_p}{\partial x}$ for Region III

	$C_{\mu 1} = .02$	$C_{\mu 1} = .057$	$C_{\mu 1} = .094$
$X_{SD} = .75h$.0019	.0045	.0038
$X_{SD} = 2.68h$.0019	.0037	.0029
$X_{SD} = 4.63h$.0018	.0044	.0029

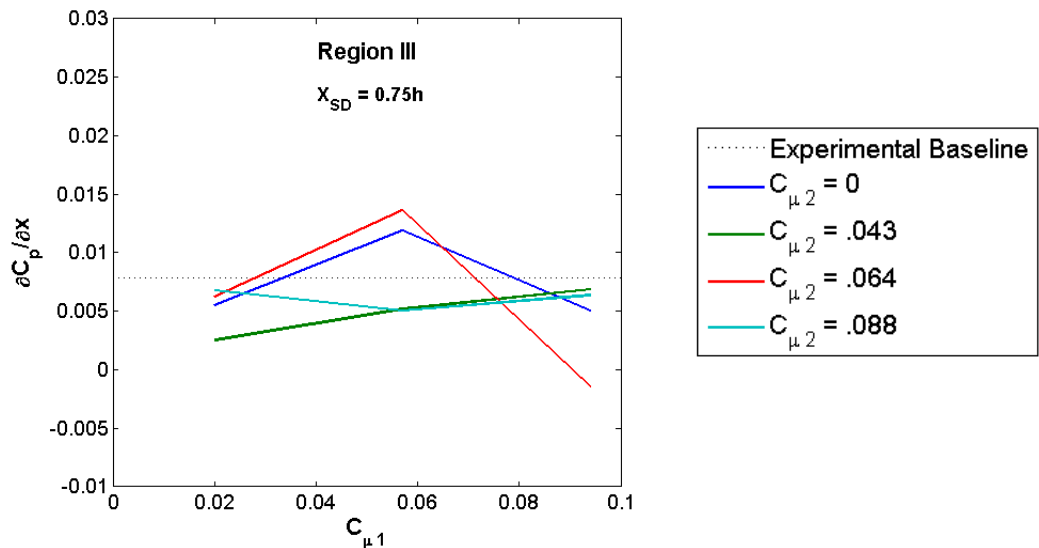


Figure 31: $X_{SD} = .75h$ – First order approximation of $\frac{\partial C_p}{\partial x}$ versus $C_{\mu 1}$ for different values of $C_{\mu 2}$ in Region III

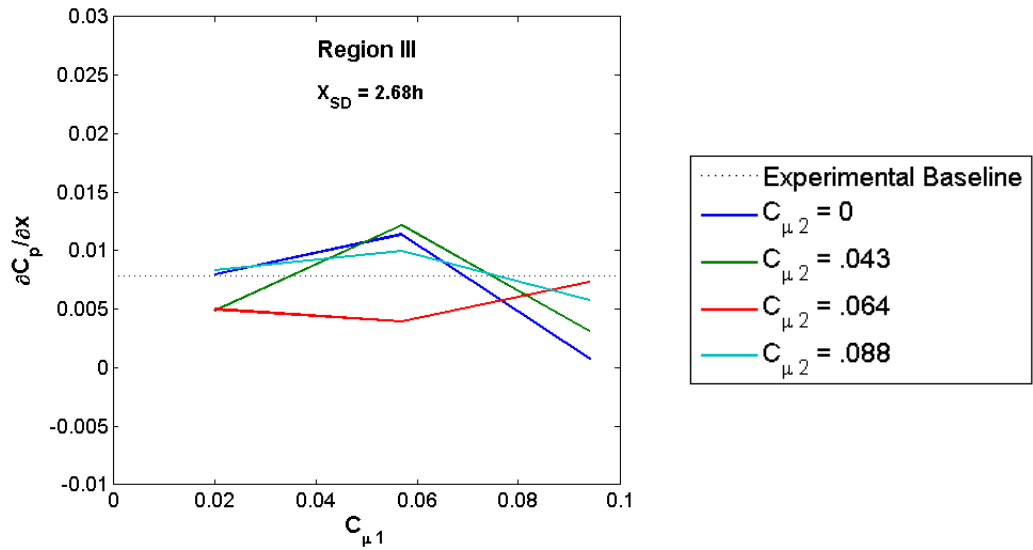


Figure 32: $X_{SD} = 2.68h$ – First order approximation of $\frac{\partial C_p}{\partial x}$ versus $C_{\mu 1}$ for different values of $C_{\mu 2}$ in Region III

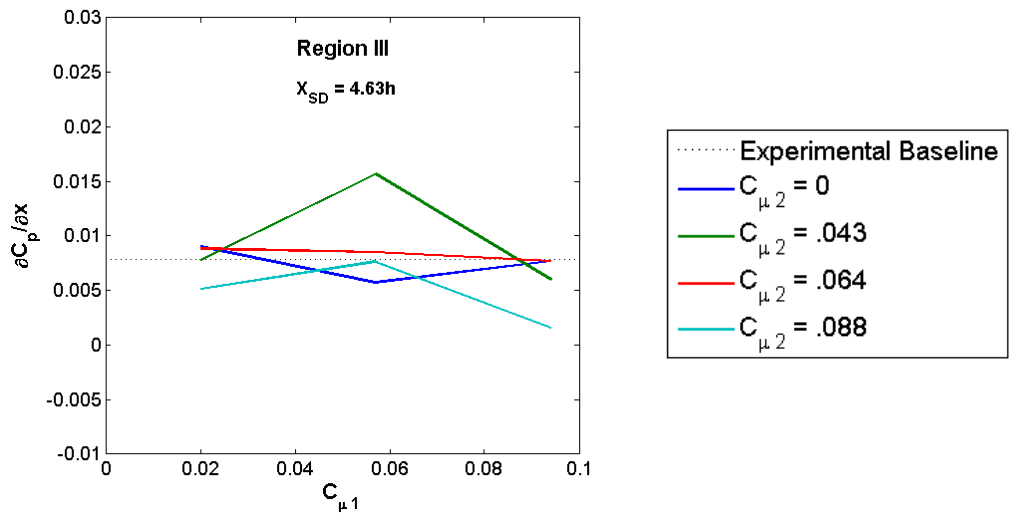


Figure 33 $X_{SD} = 4.63h$ – First order approximation of $\frac{\partial C_p}{\partial x}$ versus $C_{\mu 1}$ for different values of $C_{\mu 2}$ in Region III

4.8 Pressure Coefficient Results in Region I

Region I represents the region immediately after the point of separation, where the separated shear layer begins to develop. The pressure coefficient results from the experimental tests for Region I are shown in **Error! Reference source not found.** – 34. Before analyzing the results where both SJA1 and SJA2 are on, the case with only SJA1 on, $C_{\mu 2}=0$, is first explored in detail to identify the effects of the single actuator upstream on C_p . Focusing first on $C_{\mu 1} = .02$, the lowest momentum coefficient of SJA1 tested, it is difficult to come to any conclusion from Figure 33a as the data is limited in this region due to the location of SJA2. The same test case can be viewed more effectively in Figure 34a, & Figure 35a which both show that in Region I, $C_{\mu 1} = .02$, has very little effect on altering the flow compared to the baseline. Shifting now to study the case with the highest momentum coefficient, $C_{\mu 1} = .094$, it is perhaps more obvious looking at Figure 33b, Figure 34b, and Figure 35b as the effect of SJA1 on altering the pressure curves in Region I is more pronounced. In all three figures, the value of C_p has become more negative, which connotes that the effect of SJA1 has resulted in an increase in suction in Region I.

For the case with only SJA1 on, it can be said that the momentum coefficient of $C_{\mu 1} = .02$, is not large enough to cause a sizeable change in the streamwise pressure gradient. For the case where $C_{\mu 1} = .094$, there is an increase in suction in Region I. It follows that the momentum coefficient of $C_{\mu 1} = .094$ is high enough to cause a meaningful change in the streamwise pressure. Thus, it can be said that the

increase in suction seen in Region I is a result of the altered pressure gradient upstream of separation.

Proceeding to the cases with both of the jets on in Figures 33-35, there is a modification in the values of C_p for all cases compared to the baseline. For $X_{SD} = .75h$ there is also a change in the slope, $\frac{\partial C_p}{\partial x}$, compared to the baseline case. Based on conservation of momentum, larger Δp equates to a larger change in velocity. Applying this to the change in C_p means there is an increase in the local flow velocity in Region I. This increase in velocity can be attributed to a region of circulation close to the step, perhaps the formation of a coherent structure close to the step (a PIV study could be done to confirm this). There is a large difference between $C_{\mu 2}=0$ and $C_{\mu 2}\neq 0$ which is sufficient evidence to state that the presence of the second jet is affecting the flow beyond any local effects. As a result, the large change that is seen in $\frac{\partial C_p}{\partial x}$ stems from an interaction between the two jets and the separated shear layer. By increasing $C_{\mu 1}$ as shown in Figure 33b there is an increase in $\frac{\partial C_p}{\partial x}$ compared to the lower value shown in Figure 33a. An additional study is needed in order to better understand this.

The results of moving SJA2 to $X_{SD}=2.68h$ downstream from the step can be seen in Figure 34. In both Figure 34a-b the effect of having both SJA1 and SJA2 operating results in an increase in suction in Region I. The variations in C_p as a result of increasing $C_{\mu 2}$ are not significant enough to cause the increase in suction that appears in Figure 34. The same effect that was noted above for SJA2 located at $X_{SD} = .75h$ does not apply here. For SJA2 at $X_{SD} = 2.68h$ increasing $C_{\mu 1}$ while $C_{\mu 2}\neq 0$ results in a larger increase in suction. There is also a shift between 1.5h-2h

where $\frac{\partial C_p}{\partial x}$ begins to increase. Lastly, Figure 35 represents the extreme case of SJA2 located at $X_{SD}=4.63h$ from the step. In Figure 35a-b, the C_p curves do not vary with altering $C_{\mu 2}$ and thus are independent of $C_{\mu 2}$.

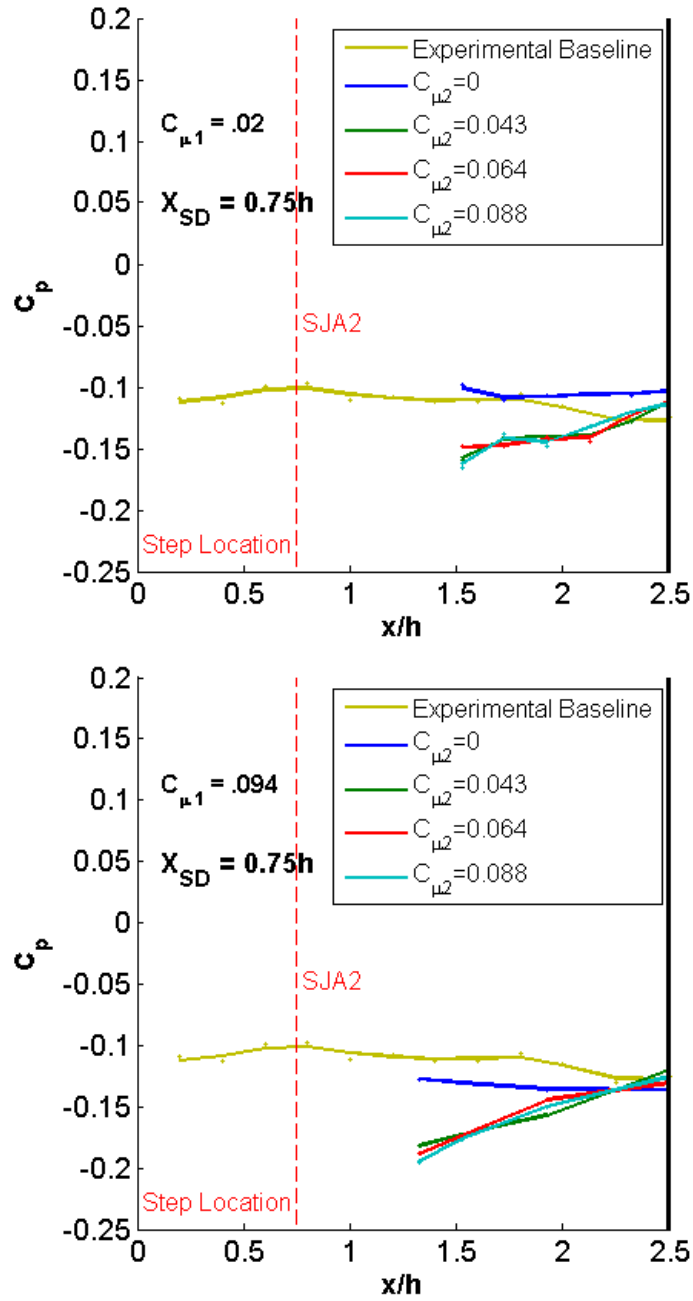


Figure 33 Region I $X_{SD} = .75h$ – Pressure coefficient downstream of step with varying momentum coefficient for SJA2, $C_{\mu 2}$. (a) Constant momentum coefficient for SJA1, $C_{\mu 2} = .02$ (b) Constant momentum coefficient for SJA1, $C_{\mu 2} = .094$.

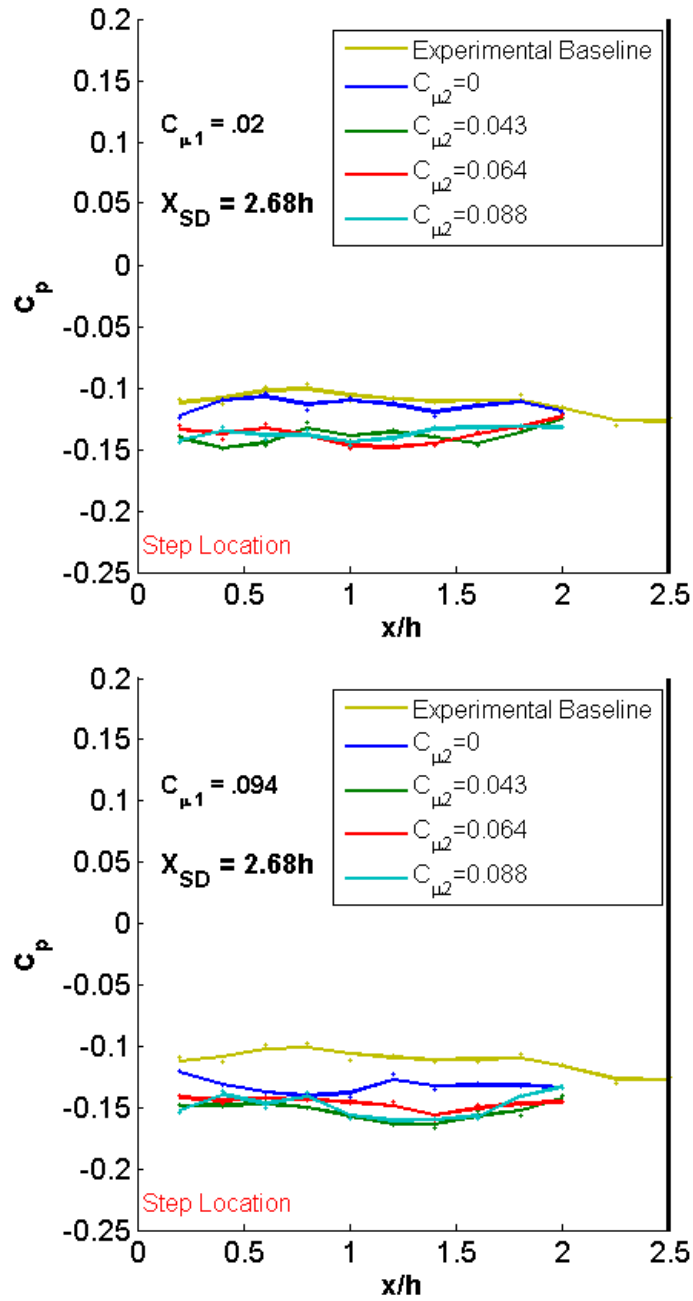


Figure 34 Region I $X_{SD} = 2.68h$ – Pressure coefficient downstream of step with varying momentum coefficient for SJA2, $C_{\mu 2}$. (a) Constant momentum coefficient for SJA1, $C_{\mu 2}=.02$ (b) Constant momentum coefficient for SJA1, $C_{\mu 2}=.094$.

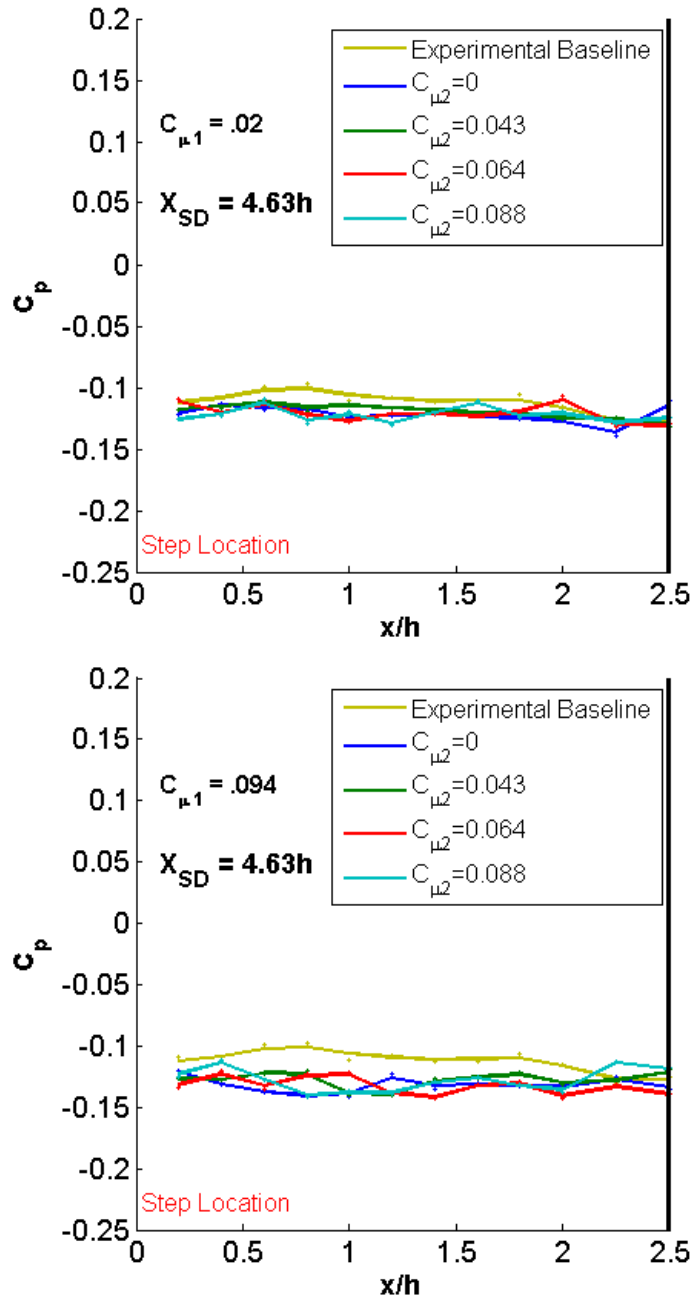


Figure 35 Region I $X_{SD} = 4.63h$ – Pressure coefficient downstream of step with varying momentum coefficient for SJA2, $C_{\mu 2}$. (a) Constant momentum coefficient for SJA1, $C_{\mu 2} = .02$ (b) Constant momentum coefficient for SJA1, $C_{\mu 2} = .094$.

4.8.1 First Order Approximation of $\frac{\partial C_p}{\partial x}$ in Region I

The slope of the pressure coefficient was estimated in Region I by performing a linear fit to the experimental data in Region I. The slope of the linear approximation is plotted against the momentum coefficient of SJA1, $C_{\mu 1}$, for the different values of $C_{\mu 2}$, the momentum coefficient of SJA2. The results are presented in Figures 36-38.

It was mentioned in the previous section that qualitatively, the effect of SJA2 at $X_{SD} = .75h$ on Region I is an increase in the suction, but more importantly there was a large difference in the slope of C_p , compared to the baseline and the case where $C_{\mu 2} = 0$. The large difference in the slope as illustrated in Figures 36-38 shows the effect of $C_{\mu 1}$ & $C_{\mu 2}$ on the slope of C_p , in Region I. The most interesting plot is Figure 36 as it illustrates the difference in the slopes for the case where $C_{\mu 2} = 0$ versus the cases where $C_{\mu 2} \neq 0$. In Figure 36 the estimated value of $\frac{\partial C_p}{\partial x}$ for $C_{\mu 2} = 0$ is very close to zero, becoming slightly negative for increasing values of $C_{\mu 1}$. In contrast to this, for all values of $C_{\mu 2} \neq 0$, $\frac{\partial C_p}{\partial x}$ is positive and increases as $C_{\mu 1}$ is increased. Lastly, the effect of varying $C_{\mu 2}$ was shown to be insignificant in the previous section, except for the case where $C_{\mu 2} = 0$ which is illustrated in Figure 36. It was mentioned in the previous section, for SJA2 located further downstream at $X_{SD} = 2.68h$ and $X_{SD} = 4.63h$, the effects in Region I are less pronounced and there was little to no change in the slope of C_p . This is again depicted in Figures 37-38; there is little variation in the estimated value of $\frac{\partial C_p}{\partial x}$ for increasing values of $C_{\mu 1}$ and for all values of $C_{\mu 2}$.

It should be noted the scatter exhibited in Figures 36-38 is an artifact of the first order approximation of the experimental data. The linear fit assumes the experimental data exhibits a linear relationship. This linear fit was performed in order to approximate the dominant features in the data and the results presented in Figures 36-38 reflect this.

The standard deviation of the first order approximation is used to further quantify the differences between the individual test cases. The results are presented below in Table 3. The values of the standard deviation for the first order approximation of $\frac{\partial c_p}{\partial x}$ for $X_{SD} = .75h$ are 3-5 times larger than those of the two other test cases. For $X_{SD} = 2.68h$ & $X_{SD} = 4.63h$, the standard deviations were found to be very similar. The results in Table 3 provide additional support to the previous narrative on the effect of X_{SD} on influencing the pressure distribution in Region I.

Table 3: Standard Deviation in 1st order Approximation of $\frac{\partial c_p}{\partial x}$ for Region I

	$C_{\mu 1} = .02$	$C_{\mu 1} = .057$	$C_{\mu 1} = .094$
$X_{SD} = .75h$.0066	.0109	.0125
$X_{SD} = 2.68h$.0020	.0041	.0023
$X_{SD} = 4.63h$.0016	.0040	.0022

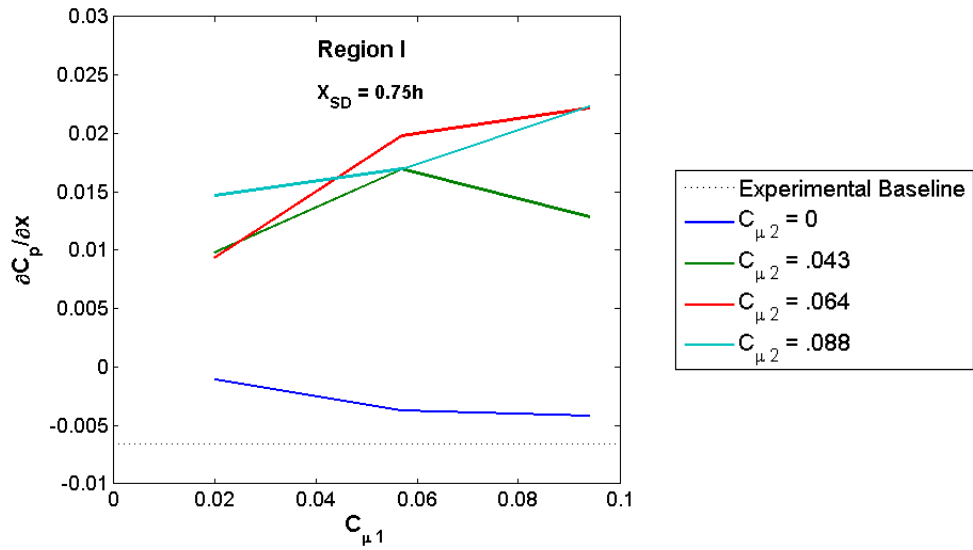


Figure 36 $X_{SD} = 0.75h$ – First order approximation of $\frac{\partial C_p}{\partial x}$ versus $C_{\mu 1}$ for different values of $C_{\mu 2}$ in Region I

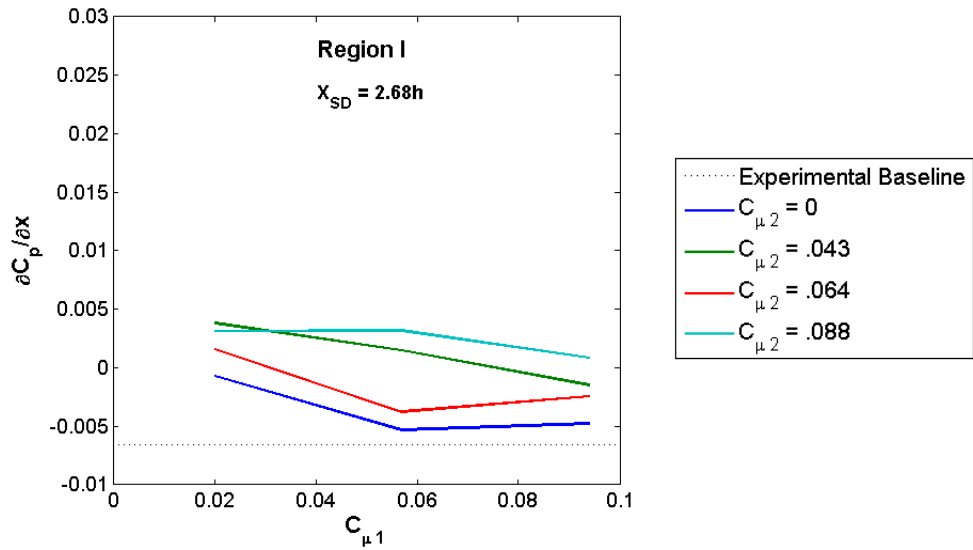


Figure 37 $X_{SD} = 2.68h$ – First order approximation of $\frac{\partial C_p}{\partial x}$ versus $C_{\mu 1}$ for different values of $C_{\mu 2}$ in Region I

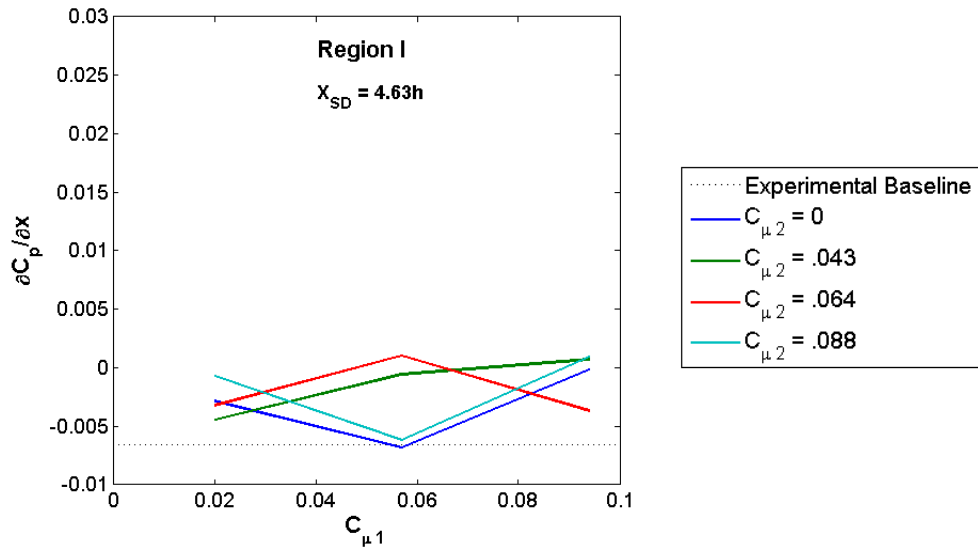


Figure 38 $X_{SD} = 4.63h$ – First order approximation of $\frac{\partial C_p}{\partial x}$ versus $C_{\mu 1}$ for different values of $C_{\mu 2}$ in Region I

4.9 Pressure Coefficient Results in Region II

We now consider Region I and Region III simply as boundary conditions for the solution represented by the data in Region II to satisfy. The boundary of Region III is invariant for all cases while the effects of the SJA1 & SJA2 in Region I have a direct effect on the flow downstream in Region II. Thus, any alteration in the shape of the C_p curve in Region I will have an impact on the shape of the curve entering Region II. In Figure 39a-b the effect is again clear; it is seemingly a continuation of the effects discussed in the previous section of Region I. The slope, $\frac{\partial C_p}{\partial x}$, appears to be different compared to the baseline case and the case without SJA2 on. Again, there is little variation in the curves for different values of $C_{\mu 2}$.

Increasing $C_{\mu 1}$ causes a larger change in the slope of the C_p curve. Figure 40a-b show similar results, though not as pronounced a change as seen in Figure 39. There is a point at which the C_p curves all converge towards the single actuator case. There is a shift in this point for the different values of $C_{\mu 1}$. This is also observed in Fig. 40a-b. There is a similarity in this point of interest between Figures 39 & 40. Figure 39a & Figure 40a both converge back to the single actuator case in the same manner; the same is true for Figure 39b & Figure 40b. A further study is necessary in order to understand the physical explanation behind this. Finally, the case where SJA2 is located downstream at $X_{SD} = 4.63h$ in Figure 41a-b is distinctly different than the cases depicted Figure 39 & Figure 40, namely that the effect of the jet location at $X_{SD} = 4.63h$ does not have any influence on the curve in Region II except in the close vicinity to the jet. This final result is significant as it represents the case where the two jets are acting independently of one another. It signifies that as SJA2 is moved as far downstream as $4.63h$ it no longer interacts with SJA1.

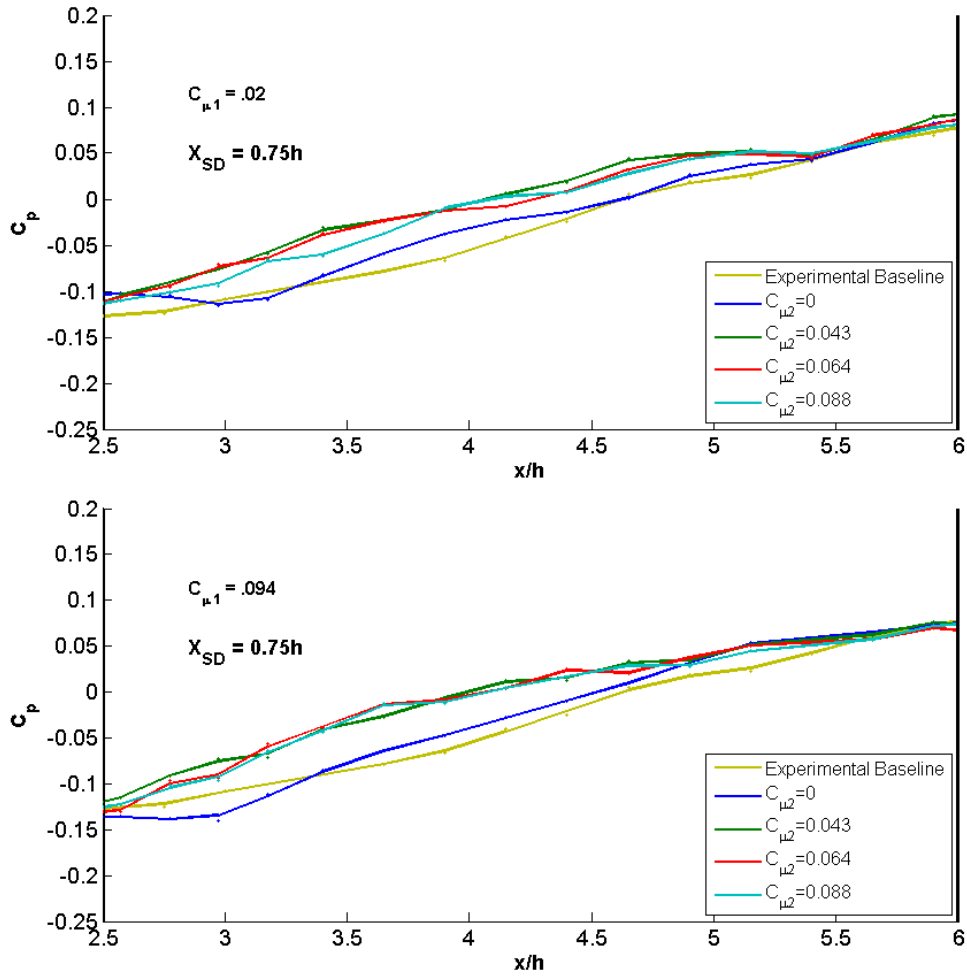


Figure 39 Region II $X_{SD} = .75h$ – Pressure coefficient downstream of step with varying momentum coefficient for SJA2, $C_{\mu 2}$. (a) Constant momentum coefficient for SJA1, $C_{\mu 2} = .02$ (b) Constant momentum coefficient for SJA1, $C_{\mu 2} = .094$.

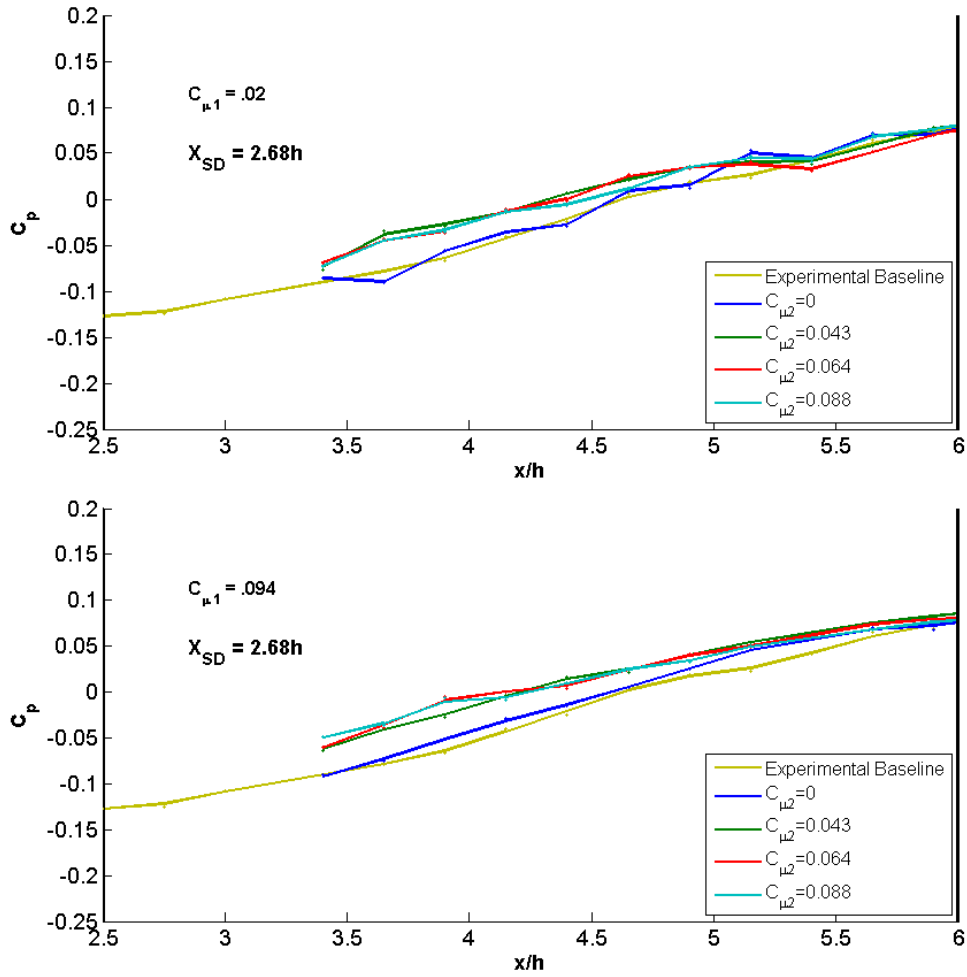


Figure 40 Region II $X_{SD} = 2.68h$ – Pressure coefficient downstream of step with varying momentum coefficient for SJA2, $C_{\mu 2}$. (a) Constant momentum coefficient for SJA1, $C_{\mu 2} = .02$ (b) Constant momentum coefficient for SJA1, $C_{\mu 2} = .094$.

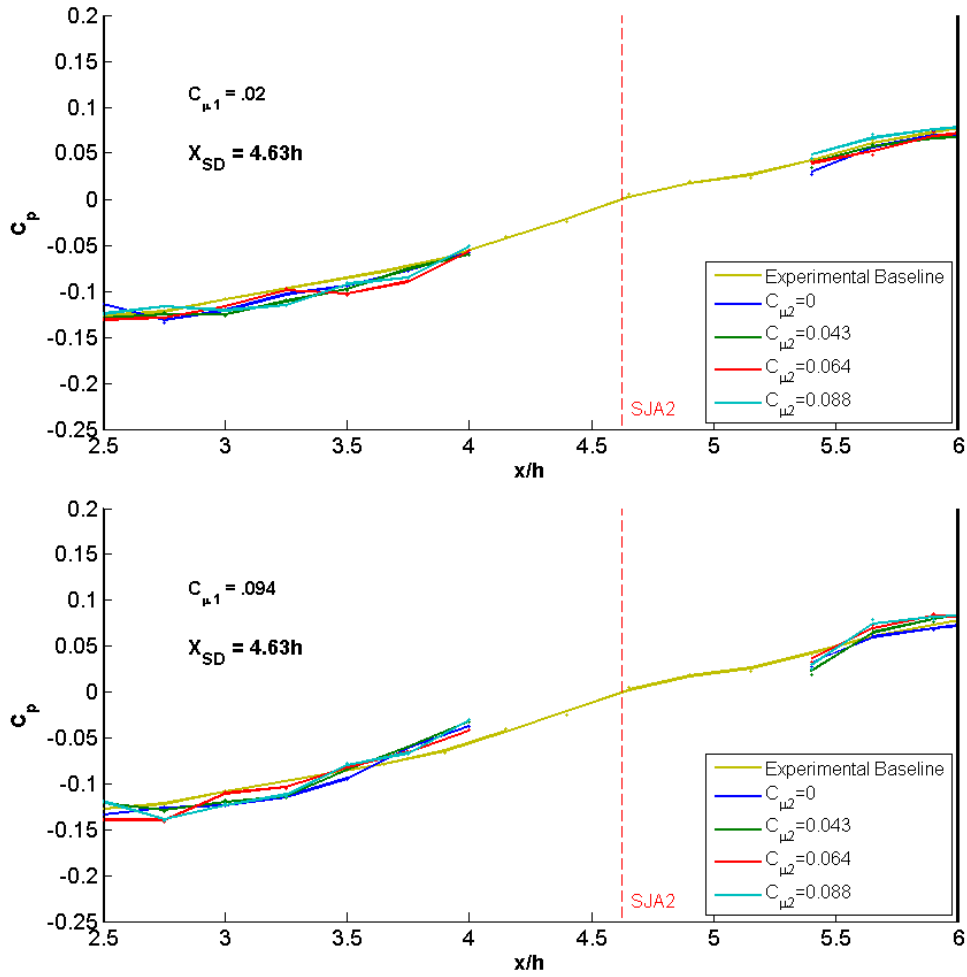


Figure 41 Region II $X_{SD} = 4.63h$ – Pressure coefficient downstream of step with varying momentum coefficient for SJA2, $C_{\mu 2}$. (a) Constant momentum coefficient for SJA1, $C_{\mu 2} = .02$ (b) Constant momentum coefficient for SJA1, $C_{\mu 2} = .094$.

4.9.1 First Order Approximation of $\frac{\partial C_p}{\partial x}$ in Region II

The slope of the pressure coefficient was estimated in Region II, by performing a linear fit to the experimental data in Region II. The experimental data in Region II was more complex than Region I due to the non-linear behavior of the data and there is also a gap in the data for SJA2 located at $X_{SD} = 2.68h$ and $X_{SD} = 4.63h$. Therefore, Region II was partitioned into two separate sections. Section 1 spanned from $2.5h - 4h$ and compared the experimental data of $X_{SD} = .75h$ and $X_{SD} = 2.68h$ while Section 2 spanned from $3.5h - 5h$ and compared the data of $X_{SD} = .75h$ and $X_{SD} = 4.63h$. Bounds for the partition of the first section, $2.5h - 4h$, were based on the experimental data available for SJA2 at $X_{SD} = 4.63h$. The test case where SJA2 was located at $X_{SD} = 2.68h$ was not included as there was not sufficient amount of data to provide a meaningful fit. The value for the lower bound for Section 2, $3.5h$, was selected as this corresponded to available data from the experimental test case where SJA2 was located at $X_{SD} = 2.68h$. The upper bound of $5h$ was selected so as to avoid the point where the graphs begin to converge towards the baseline case (as mentioned in the previous section).

The results from the first order approximation for Section 1, $2.5h-4h$, are shown in Figures 42& 43. Figures 42 & 43 illustrate the variation of $\frac{\partial C_p}{\partial x}$ versus the momentum coefficient of the upstream actuator, $C_{\mu 1}$, for different values of the downstream actuator, $C_{\mu 2}$. For Figures 42 & 43, there is little variation between the different plots of $C_{\mu 2}$, except for the case where $C_{\mu 2}=0$ in Figure 42. It was mentioned in the previous section that for SJA2 located at $X_{SD} = .75h$, increases in $C_{\mu 1}$ appeared

to result in larger changes in the slope of C_p . This trend can also be seen in Figure 42, $\frac{\partial C_p}{\partial x}$ appears to increase for increasing values of $C_{\mu 1}$. Analyzing the results shown in Figure 43, the plots appear to be very similar with very little variation. The plots show that SJA2 has very little effect as the results do not differ much from the case with $C_{\mu 2} = 0$. It can be concluded that when SJA2 is located at $X_{SD} = 4.63h$, the two jets act independently of one another.

The standard deviation of the approximated values of $\frac{\partial C_p}{\partial x}$ were calculated to quantify the variation of $\frac{\partial C_p}{\partial x}$ with respect to $C_{\mu 2}$ and $C_{\mu 1}$. The results are shown in Table 4. A comparison with the results presented in Table 4 reveals that the standard deviation of $X_{SD} = .75h$ is a full order of magnitude larger than $X_{SD} = 4.63h$.

Table 4: Standard Deviation in 1st order Approximation of $\frac{\partial C_p}{\partial x}$ for Region II – Section 1

	$C_{\mu 1} = .02$	$C_{\mu 1} = .057$	$C_{\mu 1} = .094$
$X_{SD} = .75h$.005	.0040	.0043
$X_{SD} = 4.63h$.0005	.0026	.0008

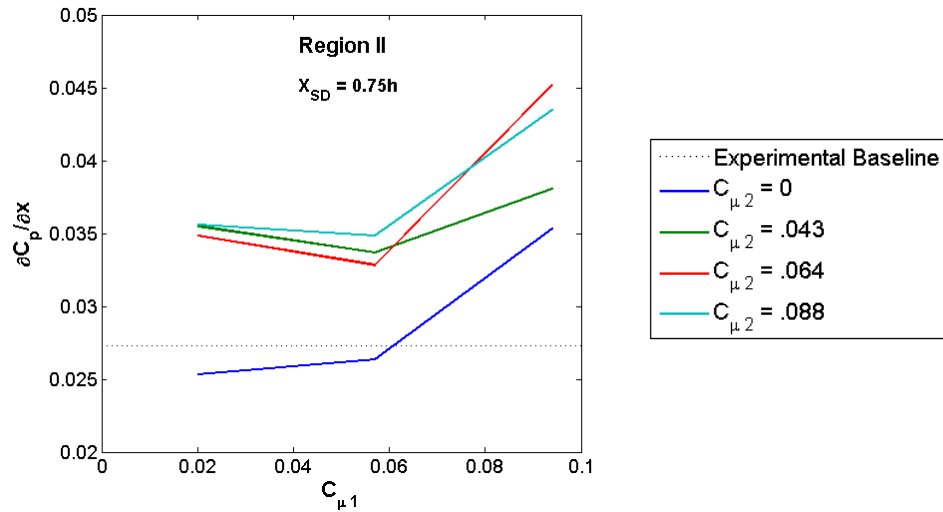


Figure 42 $X_{SD} = .75h$ – First order approximation of $\frac{\partial C_p}{\partial x}$ versus $C_{\mu 1}$ for different values of $C_{\mu 2}$ in Region II – Section 1 (2.5h-4h)

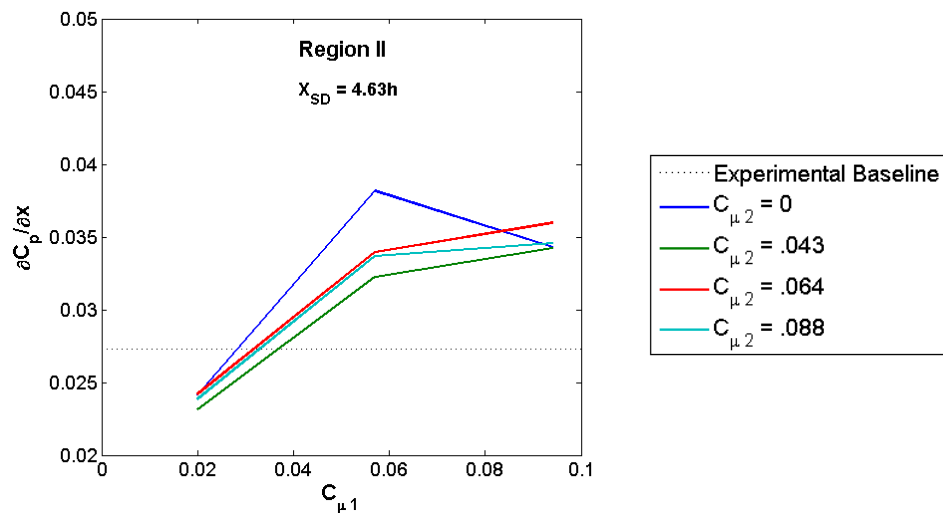


Figure 43 $X_{SD} = 4.63h$ – First order approximation of $\frac{\partial C_p}{\partial x}$ versus $C_{\mu 1}$ for different values of $C_{\mu 2}$ in Region II – Section 1 (2.5h-4h)

4.9.2 First Order Approximation of $\frac{\partial C_p}{\partial x}$ in Region II – Section 1

Similar to the previous section, the first order approximation was again calculated for Region II – Section 2. The results of the approximated values of $\frac{\partial C_p}{\partial x}$ from the linear fit are depicted in Figures 44 & 45. A comparison with the results of the pressure coefficient in Region II from SJA2 located at $X_{SD} = .75h$ & $X_{SD} = 2.63h$ displayed similar results. This

can be seen again below in Figures 44 & 45, the plots for $\frac{\partial C_p}{\partial x}$ at the two locations of X_{SD} . In both figures, the plots of $C_{\mu 2} = 0$ exhibit very different results compared to $C_{\mu 2} \neq 0$. Similarly, there is little variation in the plotted values of $\frac{\partial C_p}{\partial x}$ for different values of $\frac{\partial C_p}{\partial x} \neq 0$. Lastly, in accordance with the trend noted earlier, for increasing values of $C_{\mu 1}$, there appears to be an increasing effect on altering $\frac{\partial C_p}{\partial x}$ compared to the baseline. At first glance, looking at Figures 44 & 45, it is difficult to see such a trend in the plots.

The standard deviation of the 1st order approximation of $\frac{\partial C_p}{\partial x}$ for Region II – Section 2 can be seen in Table 5. Examining the results in Table 5 provides further confirmation for the narrative above. Specifically for $X_{SD} = .75h$, increasing the value of $C_{\mu 1}$ corresponds to larger standard deviations. This effect is also seen for $X_{SD} = 2.68h$, but again it is not as pronounced.

Table 5: Standard Deviation in 1st order Approximation of $\frac{\partial C_p}{\partial x}$ for Region II – Section 2

	$C_{\mu 1} = .02$	$C_{\mu 1} = .057$	$C_{\mu 1} = .094$
$X_{SD} = .75h$.0034	.0037	.0115
$X_{SD} = 2.68h$.0023	.0038	.0051

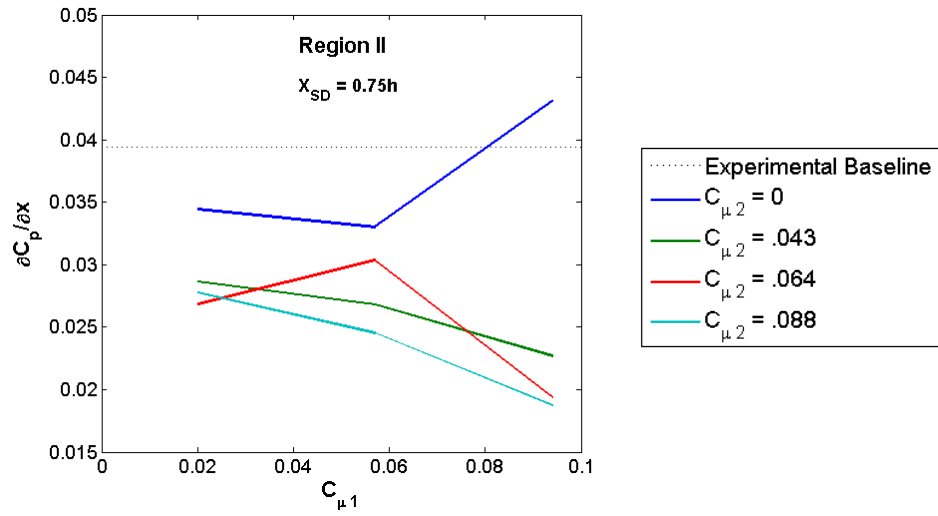


Figure 44 $X_{SD} = .75h$ – First order approximation of $\frac{\partial C_p}{\partial x}$ versus $C_{\mu 1}$ for different values of $C_{\mu 2}$ in Region II – Section 2 (3.5h-5h)

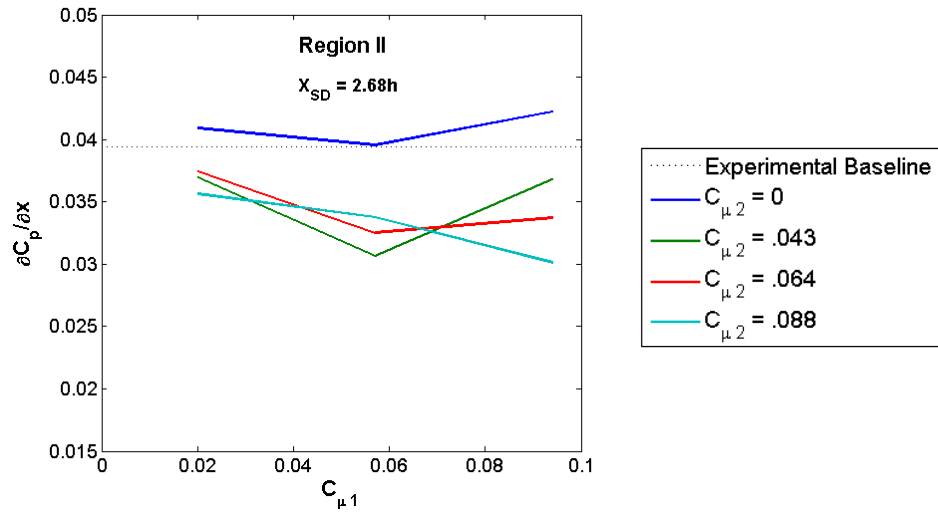


Figure 45 $X_{SD} = 2.68h$ – First order approximation of $\frac{\partial C_p}{\partial x}$ versus $C_{\mu 1}$ for different values of $C_{\mu 2}$ in Region II – Section 2 (3.5h-5h)

Chapter 5: Conclusion and Summary

Time averaged particle image velocimetry measurements showed the effect of actuator placement upstream of the step on the flow reattachment length. A single actuator placed upstream of separation has been shown to alter the streamwise pressure gradient in a manner to reduce the length of separation. Actuation at $X_S=1.07h$ reduced the reattachment length by as much as 55%. Actuation as far upstream as $7.14h$ from the step was still shown to be effective at diminishing the separation region by 24%.

Time averaged pressure data showed the ability of a second actuator placed downstream of the step to influence the pressure distribution in the wake of the step. The change in the pressure distribution in the region after the step furthers the understanding of the capability of using multiple synthetic jet actuators for virtual shaping. The effect of the second actuator on altering the downstream pressure distribution was shown to be sensitive to the location of the SJA2. It has been demonstrated that once SJA2 is located $4.63h$ downstream from the step, the jet is no longer capable of having an impact on the pressure distribution outside of the local effects of the jet. It has also been shown that an increase in momentum coefficient of SJA1, results in an increase of suction in Region I. SJA2 was also shown to cause an increase in suction in Region I and Region II for actuator locations $X_{SD} = .75h$ and $X_{SD} = 2.68h$. When SJA2 is located closest to the step, an increase in $\frac{\partial c_p}{\partial x}$ was demonstrated in Region I & Region II. This alludes to the formation of flow structures close to the step; a future PIV study is needed to study this further.

Areas for future work include PIV studies to gain insight into the flow interactions in Region I & II under the influence of SJA1 and SJA2. The effects of phase and frequency modulation were not addressed in this study, however, both have been shown to be an important parameter and will also be an interest for future work.

Appendices

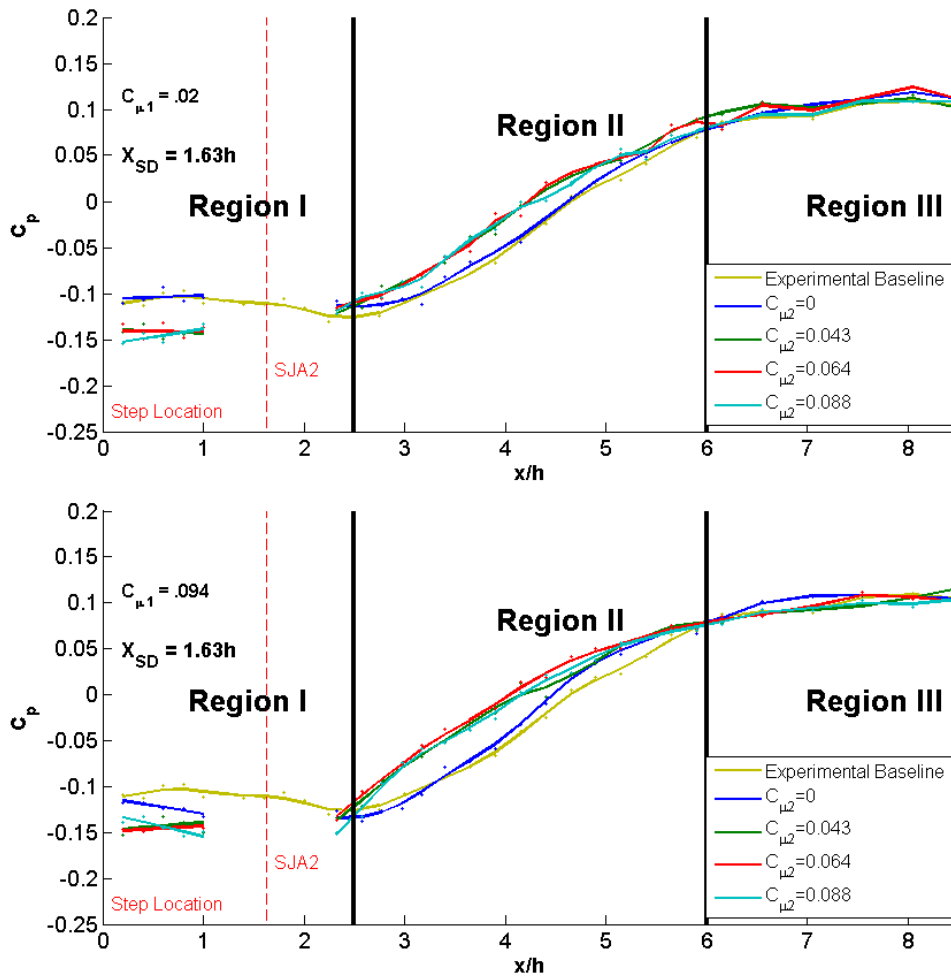


Figure 46 $X_{SD} = 1.63h$ – Pressure distribution downstream of step with varying momentum coefficient for SJA2, $C_{\mu 2}$. (a) Constant momentum coefficient for SJA1, $C_{\mu 2}=.02$ (b) Constant momentum coefficient for SJA1, $C_{\mu 2}=.094$

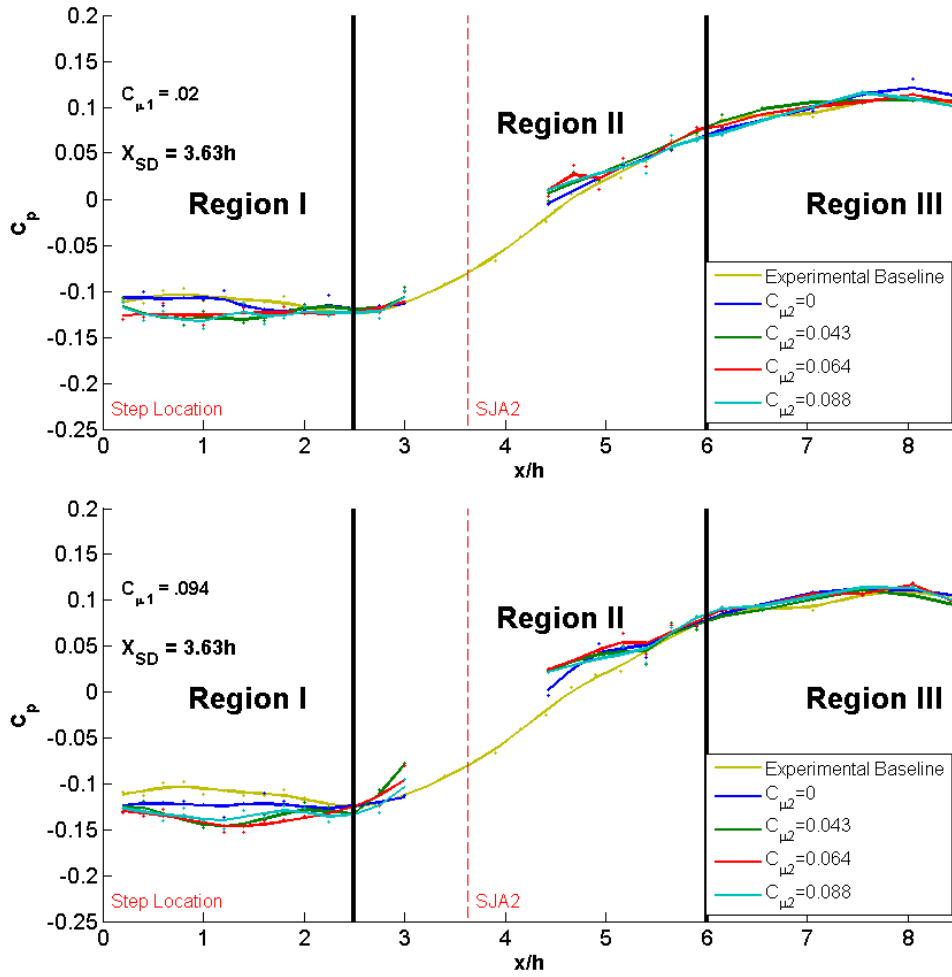


Figure 47 $X_{SD} = 3.63h$ – Pressure distribution downstream of step with varying momentum coefficient for SJA2, $C_{\mu 2}$. (a) Constant momentum coefficient for SJA1, $C_{\mu 2} = .02$ (b) Constant momentum coefficient for SJA1, $C_{\mu 2} = .094$

Bibliography

Amitay, Michael, Douglas R. Smith, Valdis Kibens, David E. Parekh, and Ari Glezer.

"Aerodynamic Flow Control over an Unconventional Airfoil Using Synthetic Jet Actuators." *AIAA Journal* 39.3 (2001): 361-70. Web.

Barlow, Jewel B., Rae, William H., and Pope, Alan, *Low-Speed Wind Tunnel*

Testing, 3rd ed., New York: John Wiley and Sons, 1999, pp. 145-146, 154-155, 164-169.

Chatlynne, E., Rumigny, N., Amitay, M., and Glezer, A., "Virtual Aero-Shaping of a Clark-Y Airfoil using Synthetic Jet Actuators", *AIAA Paper 2001-0732*, January 2001. Web.

Chen, Fang-Jenq and George Beeler (2002) "Virtual Shaping of a Two-dimensional NACA 0015 Airfoil Using Synthetic Jet Actuator." 1st Flow Control Conference

DeSalvo, Michael and Ari Glezer (2006) "Aerodynamic Control at Low Angles of Attack Using Trapped Vorticity Concentrations." 44th AIAA Aerospace Sciences Meeting and Exhibit

Desalvo, Michael, Edward Whalen, and Ari Glezer. "HIGH-LIFT ENHANCEMENT USING ACTIVE FLOW CONTROL." Hawaii. Proc. of 29th AIAA Applied Aerodynamics Conference, Honolulu. N.p., June 2011. Web.

Glezer, A. "Some Aspects of Aerodynamic Flow Control Using Synthetic-Jet Actuation." *Philosophical Transactions of the Royal Society A: Mathematical, Physical and Engineering Sciences*. 369.1940 (2011): 1476-1494. Print.

- Glezer, Ari, and Michael Amitay. "SYNTHETIC JETS." *Annual Review of Fluid Mechanics* 34 (2002): 503-29. Web.
- Glezer, Ari, Michael Amitay, and Andrew M. Honohan. "Aspects of Low- and High-Frequency Actuation for Aerodynamic Flow Control." *AIAA Journal* 43.7 (2005): 1501-511. Web.
- Greenblatt, D., and I. J. Wygnanski. "The Control of Flow Separation by Periodic Excitation." *PROGRESS IN AEROSPACE SCIENCES* 36.7 (2000): 487-545. Web.
- Hasan, M. A. Z. (1992). "The flow over a backward-facing step under controlled perturbation: laminar separation." *Journal of Fluid Mechanics*, 238, pp 73-96
doi:10.1017/S0022112092001642
- Hasnain Z., Alison Flatau, James Hubbard Jr., and Rahul Mulinti (2012) "Numerical Study and Experimental Validation of the Interaction of Multiple Synthetic Jet Actuators with Cross Flow." 50th AIAA Aerospace Sciences Meeting including the New Horizons Forum and Aerospace Exposition
- Honohan, A., Amitay, M., and Glezer, A., "Aerodynamic Control Using Synthetic Jets," AIAA Paper 2000-2401, 2000.
- Hudy, L.M., A. Naguib, W. M. Humphreys, and S. Bartram, "Particle Image Velocimetry Measurements of a Two/three-dimensional Separating/reattaching Boundary Layer Downstream of an Axisymmetric Backward-facing Step," AIAA Pap. 2005-0114 (2005), 43rd AIAA Aerospace Sciences Meeting and Exhibit, Reno, NV.

- McQuilling, M., and Jacob, J. "Effect of Chord Location on Separation Control with Vortex Generator Jets on Low Pressure Turbine Blades," AIAA-2004-2205, Presented at the 2nd AIAA Flow Control Conference, Portland, OR, June 28 - July 1, 2004.
- Rajasekaran J (2011) On the flow characteristics behind a backward facing step and a design of a new axisymmetric model from their study. Master thesis, University of Toronto
- Rumsey, L. C., "Proceedings of the 2004 Workshop on CFD Validation of Synthetic Jets and Turbulent Separation Control" NASA/CP-2007-214874
- Shea, Patrick and Douglas Smith (2009) "Aerodynamic Control of a Rectangular Wing Using Gurney Flaps and Synthetic Jets." 47th AIAA Aerospace Sciences Meeting including The New Horizons Forum and Aerospace Exposition
- Smith, Barton L., and Ari Glezer. "Vectoring of Adjacent Synthetic Jets." AIAA Journal AIAA Journal 43.10 (2005): 2117-124. Web.
- Spazzini, P. G., Di Cicca, G. M., Iuso, G., King, R., Onorato, M., "Flow Control Downstream of a Backward Facing Step: A DPIV Study", Proceedings of International Congress of Aerospace Sciences, ICAS 2002-3.9.4. Sept. 2002.
- Spazzini, P G, G Iuso, M Onorato, N Zurlo, and Cicca G. M. Di. "Unsteady Behavior of Back-Facing Step Flow." Experiments in Fluids. 30.5 (2001): 551. Print.
- Ugrina, Sandra. "Experimental Analysis and Analytical Modeling of Synthetic Jet Cross Flow Interactions" Dissertation University of Maryland, 2007.

Yamada, S., Okamoto, K., Nitta, T., Motosuke, M., and Honmami, S. (2009) "Flow Structures by Synthetic Jets Over a Backward Facing Step in Low Reynolds Number." 47th AIAA Aerospace Sciences Meeting including The New Horizons Forum and Aerospace Exposition:

Y. Liu, W. Kang, and H. J. Sung, "Assessment of the organization of a turbulent separated and reattaching flow by measuring wall pressure fluctuations," Experiments in Fluids, vol. 38, pp. 485-493, 2005.